

Performance Bounds and Optimization for CSI-Ratio based Bi-static Doppler Sensing in ISAC Systems

Yanmo Hu, *Student Member, IEEE*, Kai Wu, *Member, IEEE*,
J. Andrew Zhang, *Senior Member, IEEE*, Weibo Deng, Y. Jay Guo, *Fellow, IEEE*

Abstract—Bi-static sensing is crucial for exploring the potential of networked sensing capabilities in integrated sensing and communications (ISAC). However, it suffers from the challenging clock asynchronism issue. CSI ratio-based sensing is an effective means to address the issue. Its performance bounds, particular for Doppler sensing, have not been fully understood yet. This work endeavors to fill the research gap. Focusing on a single dynamic path in high-SNR scenarios, we derive the closed-form CRB. Then, through analyzing the mutual interference between dynamic and static paths, we simplify the CRB results by deriving close approximations, further unveiling new insights of the impact of numerous physical parameters on Doppler sensing. Moreover, utilizing the new CRB and analyses, we propose novel waveform optimization strategies for noise- and interference-limited sensing scenarios, which are also empowered by closed-form and efficient solutions. Extensive simulation results are provided to validate the preciseness of the derived CRB results and analyses, with the aid of the maximum-likelihood estimator. The results also demonstrate the substantial enhanced Doppler sensing accuracy and the sensing capabilities for low-speed target achieved by the proposed waveform design.

Index Terms—Integrated sensing and communication (ISAC), Perceptive mobile networks, uplink sensing, CSI-ratio model, Cramér-Rao bounds, OFDM symbol optimization.

I. INTRODUCTION

INTEGRATED sensing and communications (ISAC) has established its critical role in numerous next-generation communication networks, such as mobile networks, WiFi networks and vehicular networks etc [1]–[6]. Major sensing types extensively discussed in ISAC include single-node sensing with sensing transceivers co-located and bi-static sensing with sensing transmitters far separated from receivers. While single-node sensing enjoy clock coherence between transceiver channels, it requires full-duplex technique, which is not mature yet [7]. Bi-static sensing can eliminate the requirement of full-duplexing techniques and has the potential to utilize the networked sensing capability to deliver enhanced sensing performances [8], [9]. Take the emerging perceptive mobile networks (PMNs) [10] for an example. Bi-static sensing at a

base station using the link signals from almost ubiquitous user ends can enjoy unprecedented spatial diversity and information fusion gain for sensing. However, such bi-static sensing is not without challenges. Due to different clock oscillators, between transmitter and receiver, bi-static sensing suffers from the clock asynchronism issue [7], [11], [12]. It can lead to sensing ambiguities and must be solved for fully enjoying the potential networked sensing ISAC.

Several types of methods have been proposed to solve the clock asynchronism issue in ISAC. Since the antennas at a communication receiver typically share a common clock source, the signals received by each antenna have the same timing and phase nuisances caused by clock asynchronism. Leveraging this characteristic, the cross-antenna cross-correlation (CACC) methods were proposed in [13], [14], which compensate clock asynchronism errors by taking the cross-correlations of the received signals over different antenna pairs. However, the CACC method doubles the sensing parameters that need to be estimated and increases the probability of detecting false dynamic targets (also known as ghost targets). Moreover, the CACC method requires a line-of-sight (LOS) path to ensure unambiguous sensing. In practical scenarios, the LOS requirement may not be easy to be satisfied.

The CSI-ratio model [15]–[17], a counterpart of CACC, has the ability to alleviate the LOS requirement. Different from CACC, the CSI-ratio model calculates the ratio of signals among different antennas to eliminate common errors caused by clock asynchronism. In [16], the Doppler frequency of a single dynamic target is estimated by employing the Mobius transformation, which constructs a periodic conformal map between CSI ratio and Doppler frequency. The Doppler frequency can be estimated by calculating the period of the CSI ratio. Furthermore, [17] introduces the MUSIC algorithm to the CSI-ratio-based sensing. Compared with the CACC-based MUSIC method, the CSI-ratio-based MUSIC has better performance in estimating delay and Doppler in both LOS and NLOS scenarios [7], [15]. Therefore, as an elegant formulation, the CSI ratio model allows simple and efficient parameter estimation. It also has the capability of removing additional common signal distortions across antennas such as varying receiver gains [15], remarkably standing out from algorithms for solving the clock asynchronism issue.

Despite advancements of the CSI-ratio model, assessing its optimality remains unsolved and signal optimization lacks of reliable performance metrics. In parameter estimation, the

Yanmo Hu and Weibo Deng are with the Key Laboratory of Marine Environmental Monitoring and Information Processing, Ministry of Industry and Information Technology, and also with the School of Electronic and Information Engineering, Harbin Institute of Technology. Email: 19B905008@stu.hit.edu.cn; dengweibo@hit.edu.cn. (*Corresponding author: Weibo Deng.*)

Kai Wu, J. A. Zhang and Y. J. Guo are with Global Big Data Technologies Centre, the University of Technology Sydney. Email: {Kai.Wu; Andrew.Zhang; Jay.Guo}@uts.edu.au.

classical Cramér-Rao bounds (CRB), as the lower bound of the variance of an unbiased estimator, is an effective metric for assessing the optimality of an estimator and signal design [18]. However, CRB for the CSI-ratio model, and more generally for bi-static sensing, is not known yet, although limited works have studied the CRB for ISAC without clock asynchronism [19]–[22]. For downlink sensing, [19] optimizes the subcarrier and OFDM symbol indexes to minimize delay and Doppler frequency CRBs, respectively. Additionally, [22] minimizes the closed-form CRB to improve delay estimation accuracy in 5G NR networks [23]. In [21], an uplink waveform optimization problem is solved with the synchronized clock assumption. An algorithm is proposed to jointly optimize the subcarrier indexes and the power allocation to enhance the estimation accuracy. These studies highlight the importance of CRB in performance analysis and optimization in ISAC. However, it is very challenging to derive meaningful CRB results for bi-static sensing with clock asynchronism, due to the multiple unknown time-varying variables of offsets.

To contribute to filling the research gap in the literature, this paper is dedicated to analyzing and optimizing the Doppler CRB for CSI ratio-based bi-static sensing in ISAC. We start with deriving the analytical CRB under high-signal-to-noise-ratio (SNR) scenarios. Then, utilizing the interference pattern between dynamic and static paths, we provide an approximated CRB, which not only closely approaches the exact CBR but also reveals impact of critical physical quantities on Doppler sensing. Moreover, employing the derived CBR and the unveiled insights through CRB analysis, we propose new waveform design to optimize the Doppler sensing performance in CSI ratio-based bi-static sensing. The major contributions are highlighted as follows:

- We derive the closed-form CRB for Doppler sensing employing the CSI-ratio model for bi-static sensing in high-SNR scenarios for a single dynamic path. Through analyzing the impact of mutual impact between dynamic and static paths, we manage to simplify the closed-form CRB by deriving a close CRB approximation.
- We perform extensive analysis employing the derived CRB results, unveiling new and interesting insights into the impact of different parameters, such as average power of static and dynamic paths, incident angles of static and dynamic paths, and noise power etc., on Doppler sensing performances.
- We provide new waveform design to optimize Doppler sensing performance in different bi-static sensing scenarios, utilizing the preceding CRB results and analyses. For noise-limited cases, where interference between dynamic and static paths can be ignored, we derive the optimal waveform for Doppler sensing. Moreover, for interference-limited sensing, we develop a novel waveform optimization strategy to enhance the region of sensible Doppler frequencies, particularly for small values. The strategy also entails an optimal trade-off between interference- and noise-limited Doppler sensing.

Extensive simulation results are provided to demonstrate the validity of the CRB results and analyses. A maximum

likelihood estimator is used to validate the derived CRBs. Impact of different parameters on CRBs is also simulated, to consolidate the analyses. We also validate the preciseness of the new derivations and analyses, as well as the optimality of the proposed waveform design.

The rest of the paper is organized as follows. Section II introduces the signal model of the CSI-ratio. The derivation of CRB of the CSI-ratio model and the analysis of the Doppler CRB are presented in Section III. Section IV proposes two algorithms to enhance the model accuracy by optimizing indexes of the OFDM symbols. Simulation results are provided in Section V, and conclusions are drawn in Section VI.

Notation: \odot denotes the Hadamard product; if $\mathbf{a} \in \mathbb{C}^{N \times 1}$ is a vector, $|\mathbf{a}|$, $|\mathbf{a}|^2$, and \mathbf{a}^2 denote the absolute value, the square of the absolute value, and the square value of each element in \mathbf{a} ; $[\mathbf{a}]_n$ denotes the n -th element of vector \mathbf{a} , and $[\mathbf{A}]_{m,n}$ denotes the (m, n) -th element of matrix \mathbf{A} ; if $\mathbf{a}, \mathbf{b} \in \mathbb{C}^{N \times 1}$ are vectors, \mathbf{a}/\mathbf{b} denotes the division of the corresponding elements in two vectors, where $[\mathbf{a}/\mathbf{b}]_n = a_n/b_n, n = 0, \dots, N-1$; $\angle a$ denotes the argument of the complex number $a \in \mathbb{C}$; $\text{round}\{a\}$ denotes the rounding operation for $a \in \mathbb{R}$; $C_n^r = \frac{n!}{r!(n-r)!}$ denotes the combinatorial number; $\mathcal{F}\{\cdot\}$ is the discrete Fourier transform (DFT) operator; $\text{sinc}(x) = \sin(\pi x)/(\pi x)$ is the sinc function.

II. CSI-RATIO MODEL

In PMN ISAC, uplink sensing generally suffers from clock asynchronism issues [1], [7]. Specifically, the clock offset between transmitter and receiver incurs TMO and CFO, which further leads to the Doppler and delay ambiguity. Thus, the TMO and CFO compensation is essential for uplink sensing. One effective method for eliminating CFO and TMO is based on the CSI ratio between different receiving antennas. Additionally, we assume that the TMO and CFO remain constants within each OFDM symbol [7], and we use $\tau_{o,k}$ and β_k to denote the TMO and CFO of the k -th OFDM symbol.

In 5G NR, the OFDM symbols in physical uplink shared channel (PUSCH) can be designed for improving the sensing performance [24], [25]. Therefore, we consider a general case that the interval of adjacent OFDM symbols for sensing can be unequal, and the symbol interval is an integer multiple of T_0 . We use K_{all} to represent the number of the available OFDM symbols. Suppose that K out of K_{all} OFDM symbols are allocated for the uplink sensing, and the index of the k -th sensing symbol is $\varphi_k \in \mathbb{Z}$, where $0 \leq \varphi_k \leq K_{\text{all}} - 1$ with $k = 0, \dots, K - 1$. The sensing receiver at the BS uses a uniform linear array. Let Δf denote the subcarrier interval. Moreover, we consider that there are L_s static objects (with AOA $\theta_{s,\ell}$ and delay $\tau_{s,\ell}$) and one dynamic path associated with a moving target (with the Doppler frequency f_d , AOA θ_d , and delay τ_d). Accordingly, the CSI for the p -th subcarrier of the k -th OFDM symbol and the m -th antenna of the BS can be expressed as [1]:

$$y_{p,k}^{(m)} = e^{j\beta_k} e^{j2\pi p \Delta f \tau_{o,k}} \left(\xi_d e^{j2\pi p \Delta f \tau_d} e^{j \frac{2\pi}{\lambda} d_m \sin \theta_d} e^{j2\pi \varphi_k f_d T_0} + \sum_{\ell=0}^{L_s-1} \xi_{s,\ell} e^{j2\pi p \Delta f \tau_{s,\ell}} e^{j \frac{2\pi}{\lambda} d_m \sin \theta_{s,\ell}} \right) + z_{p,k}^{(m)}, \quad (1)$$

where ξ_d and $\xi_{s,\ell}$ denote the combined value of the complex-valued reflection coefficient and the propagation attenuation for the dynamic target and the ℓ -th static object, respectively; λ denotes the wavelength; d_m denotes the position of the m -th antenna; $z_{p,k}^{(m)} \sim \mathcal{CN}(0, \sigma_n^2)$ is the Gaussian noise.

The CSI ratio between two different receiving antennas can effectively eliminate the impact of the clock offset [15]. Therefore, we consider a simple two-element array, $M = 2$, with d denoting the spacing between the two elements and $a(\theta_d) = e^{j\frac{2\pi}{\lambda}d\sin\theta_d}$ denoting the phasor caused by the phase difference between two array elements. The CSI ratio can be calculated as:

$$r(k) = y_k^{(1)}/y_k^{(0)} = \frac{a(\theta_d)\rho_1^{(p)}e^{j2\pi\varphi_k f_d T_0} + \rho_0^{(p)} + (\tilde{z}_{p,k}^{(1)}/h_{s,0}^{(p)})}{\rho_1^{(p)}e^{j2\pi\varphi_k f_d T_0} + 1 + (\tilde{z}_{p,k}^{(0)}/h_{s,0}^{(p)})}, \quad (2)$$

where $\xi_d^{(p)} \triangleq \xi_d e^{j2\pi p \Delta f \tau_d}$, $\xi_{s,\ell}^{(p)} \triangleq \xi_{s,\ell} e^{j2\pi p \Delta f \tau_{s,\ell}}$, $\tilde{z}_{p,k}^{(0)} \triangleq e^{-j\beta_k} e^{-j2\pi p \Delta f \tau_{o,k}} z_{p,k}^{(0)}$, $\tilde{z}_{p,k}^{(1)} \triangleq e^{-j\beta_k} e^{-j2\pi p \Delta f \tau_{o,k}} z_{p,k}^{(1)}$, and four key intermediate variables are defined as

$$\rho_0^{(p)} = \frac{h_{s,1}^{(p)}}{h_{s,0}^{(p)}}, \quad \rho_1^{(p)} = \frac{\xi_d^{(p)}}{h_{s,0}^{(p)}} \\ h_{s,0}^{(p)} = \sum_{\ell=0}^{L_s-1} \xi_{s,\ell}^{(p)}, \quad h_{s,1}^{(p)} = \sum_{\ell=0}^{L_s-1} \xi_{s,\ell}^{(p)} e^{j\frac{2\pi}{\lambda}d\sin\theta_{s,\ell}}. \quad (3)$$

As is typical [16], we employ the uplink signal from *the same subcarrier in each OFDM symbol for Doppler sensing*. The analysis in this work can be readily applicable to any subcarrier. Hence, we omit the subcarrier index p of all variables, and ρ_0 , ρ_1 , $h_{s,0}$, $h_{s,1}$, ξ_d , $\xi_{s,\ell}$, $\tilde{z}_{p,k}^{(0)}$, $\tilde{z}_{p,k}^{(1)}$ are re-expressed as ρ_0 , ρ_1 , $h_{s,0}$, $h_{s,1}$, ξ_d , $\xi_{s,\ell}$, $\tilde{z}_k^{(0)}$, $\tilde{z}_k^{(1)}$, respectively.

The terms $h_{s,0}$ and $h_{s,1}$ denote the static part in the received signals from the 0-th and 1-st antennas, respectively. Both the numerator and denominator of (2) have terms related to Gaussian noises, and the CSI ratio expression is nonlinear. Therefore, the probability density function of (2) is too complicated to be derived for calculating the CRB [26]. As a typical strategy, we introduce a legitimate assumption, i.e., high SNR, to simplify the derivation of the CRB and then evaluate the impact of the assumption later in Section V-A. Considering the *high-SNR case*, the CSI ratio can be approximated using the Taylor series expansion, as given by:

$$r(k) \approx \frac{a(\theta_d)\rho_1 e^{j2\pi\varphi_k f_d T_0} + \rho_0}{\rho_1 e^{j2\pi\varphi_k f_d T_0} + 1} + \frac{\tilde{z}_k^{(1)}/h_{s,0}}{\rho_1 e^{j2\pi\varphi_k f_d T_0} + 1} - \frac{a(\theta_d)\rho_1 e^{j2\pi\varphi_k f_d T_0} + \rho_0}{(\rho_1 e^{j2\pi\varphi_k f_d T_0} + 1)^2} \left(\tilde{z}_k^{(0)}/h_{s,0} \right). \quad (4)$$

Note that the approximation holds when the noise term $\tilde{z}_k^{(1)}/h_{s,0}$ and $\tilde{z}_k^{(0)}/h_{s,0}$ in (2) are much smaller than other components. The more specific conditions of the approximation can be established as follows.

Lemma 1. *If $|\xi_d| < \min\{|h_{s,0}|, |h_{s,1}|\}$, the approximation in (4) holds when:*

$$\min\{|h_{s,0}|, |h_{s,1}|\} - |\xi_d| \gg \sigma_n. \quad (5)$$

If $|\xi_d| > \max\{|h_{s,0}|, |h_{s,1}|\}$, the approximation holds when:

$$|\xi_d| - \max\{|h_{s,0}|, |h_{s,1}|\} \gg \sigma_n. \quad (6)$$

For convenience of incorporating all sensing symbols in the CRB analysis, we introduce the matrix form of the CSI ratio below. With the symbol interval T_0 , the Doppler steering vector can be given by

$$\mathbf{d}(f_d) = [e^{j2\pi\varphi_0 f_d T_0}, \dots, e^{j2\pi\varphi_{K-1} f_d T_0}]^T \in \mathbb{C}^{K \times 1}.$$

Note that φ_k is the symbol index and may not be evenly distributed in our analysis. Moreover, let the vectors $\tilde{\mathbf{z}}^{(0)} = [\tilde{z}_0^{(0)}, \dots, \tilde{z}_{K-1}^{(0)}]^T h_{s,0}^{-1} \in \mathbb{C}^{K \times 1}$ and $\tilde{\mathbf{z}}^{(1)} = [\tilde{z}_0^{(1)}, \dots, \tilde{z}_{K-1}^{(1)}]^T h_{s,0}^{-1} \in \mathbb{C}^{K \times 1}$ denote the noise vectors of the 0-th and the 1-st antennas with respect to K numbers of OFDM symbols, respectively. Based on (4), the vector of CSI ratios over all sensing symbols can be written as:

$$\mathbf{r} = \frac{a(\theta_d)\rho_1 \mathbf{d}(f_d) + \rho_0 \mathbf{1}_{K \times 1}}{\rho_1 \mathbf{d}(f_d) + \mathbf{1}_{K \times 1}} \triangleq \underbrace{\mathbf{x}}_{\mathbf{x}} + \underbrace{\frac{\tilde{\mathbf{z}}^{(1)}}{\rho_1 \mathbf{d}(f_d) + \mathbf{1}_{K \times 1}} - \frac{a(\theta_d)\rho_1 \mathbf{d}(f_d) + \rho_0 \mathbf{1}_{K \times 1}}{(\rho_1 \mathbf{d}(f_d) + \mathbf{1}_{K \times 1})^2} \odot \tilde{\mathbf{z}}^{(0)}}_{\mathbf{z}} \triangleq \boldsymbol{\chi} + \mathbf{z}. \quad (7)$$

From (4), we can verify that $r(k)$ has a Gaussian distribution with the mean of $\boldsymbol{\chi}$ and variance of $\text{diag}\{\boldsymbol{\eta}\}$, where

$$\boldsymbol{\eta} = \frac{\sigma_n^2}{|h_{s,0}|^2} \frac{|\rho_1 \mathbf{d}(f_d) + \mathbf{1}_{K \times 1}|^2 + |a(\theta_d)\rho_1 \mathbf{d}(f_d) + \rho_0 \mathbf{1}_{K \times 1}|^2}{|\rho_1 \mathbf{d}(f_d) + \mathbf{1}_{K \times 1}|^4}.$$

Hence, \mathbf{r} conforms to a joint Gaussian distribution, as given by $\mathbf{r} \sim \mathcal{CN}(\boldsymbol{\chi}, \text{diag}\{\boldsymbol{\eta}\})$. Next, we employ these signal models to investigate the Doppler sensing performance using CSI ratio.

III. CRB FOR CSI-RATIO-BASED SENSING

In this section, we first derive the closed-form CRB for CSI ratio-based Doppler sensing and then analyze the result to highlight some insights.

A. Deriving CRB

The CRB derivation is based on the CSI ratio vector \mathbf{r} , as given in (7). Let us collect the unknown parameters in (7) by the following real vector:

$$\boldsymbol{\alpha} = [f_d, \theta_d, \text{Re}\{\rho_0\}, \text{Im}\{\rho_0\}, \text{Re}\{\rho_1\}, \text{Im}\{\rho_1\}]^T \in \mathbb{R}^{6 \times 1}, \quad (8)$$

where ρ_0 and ρ_1 are given in (3). As is typical, the CRB derivation is started with establishing the Fisher information matrix (FIM) [18]. Let $\mathbf{F}(\boldsymbol{\alpha}) \in \mathbb{R}^{6 \times 6}$ denote the FIM. The (p, q) -th entry can be given by:

$$[\mathbf{F}(\boldsymbol{\alpha})]_{p,q} = 2 \text{Re} \left\{ \left(\frac{\partial \boldsymbol{\chi}}{\partial [\boldsymbol{\alpha}]_p} \right)^H \text{diag}^{-1}\{\boldsymbol{\eta}\} \frac{\partial \boldsymbol{\chi}}{\partial [\boldsymbol{\alpha}]_q} \right\}$$

$$\begin{aligned}
\gamma_{11} &= \frac{\varepsilon_1 |\varepsilon_{d,K,\mu}|^2 - 2\varepsilon_{K,1} \operatorname{Re} \left\{ \varepsilon_{d,K,\mu}^* \varepsilon_{d,\mu,1} \right\} + \varepsilon_{\mu,2} \varepsilon_{K,1}^2}{\varepsilon_1 \varepsilon_{\mu,2} - |\varepsilon_{d,\mu,1}|^2}, \quad \gamma_{22} = \frac{\varepsilon_1 |\varepsilon_{d,\mu,2}|^2 - 2\operatorname{Re} \left\{ \varepsilon_{d,\mu,2}^* \varepsilon_{d,\mu,1} \varepsilon_{\mu,1}^* \right\} + \varepsilon_{\mu,2} |\varepsilon_{\mu,1}|^2}{\varepsilon_1 \varepsilon_{\mu,2} - |\varepsilon_{d,\mu,1}|^2}, \\
\gamma_{12} &= \left(\varepsilon_1 \varepsilon_{\mu,2} - |\varepsilon_{d,\mu,1}|^2 \right)^{-1} \operatorname{Im} \left\{ \rho_2^* \varepsilon_{d,\mu,2} (\varepsilon_1 \varepsilon_{d,K,\mu} - \varepsilon_{K,1} \varepsilon_{d,\mu,1}) + \rho_2^* \varepsilon_{\mu,1} (\varepsilon_{K,1} \varepsilon_{\mu,2} - \varepsilon_{d,\mu,1}^* \varepsilon_{d,K,\mu}) \right\}, \\
\mathbf{\Lambda} &= \operatorname{diag}^{-1} \left\{ |\boldsymbol{\mu}|^2 + |a(\theta_d) \rho_1 \mathbf{d}(f_d) + \rho_0 \mathbf{1}_{K \times 1}|^2 \right\} \in \mathbb{R}^{K \times K}, \quad \boldsymbol{\mu} = \rho_1 \mathbf{d}(f_d) + \mathbf{1}_{K \times 1} \in \mathbb{C}^{K \times 1}, \quad \boldsymbol{\varphi} = [\varphi_0, \dots, \varphi_{K-1}]^T \in \mathbb{Z}^{K \times 1}, \\
\varepsilon_1 &= \mathbf{1}_{K \times 1}^T \mathbf{\Lambda} \mathbf{1}_{K \times 1} \in \mathbb{R}, \quad \varepsilon_{K,1} = (2\pi T_0) \mathbf{1}_{K \times 1}^T \mathbf{\Lambda} \boldsymbol{\varphi} \in \mathbb{R}, \quad \varepsilon_{K,2} = (2\pi T_0)^2 \mathbf{1}_{K \times 1}^T \mathbf{\Lambda} \boldsymbol{\varphi}^2 \in \mathbb{R}, \quad \varepsilon_{\mu,2} = \mathbf{1}_{K \times 1}^T \mathbf{\Lambda} |\boldsymbol{\mu}|^2 \in \mathbb{R}, \\
\varepsilon_{\mu,1} &= \left(\frac{\partial a(\theta_d)}{\partial \theta_d} \right) \mathbf{1}_{K \times 1}^T \mathbf{\Lambda} \boldsymbol{\mu} \in \mathbb{C}, \quad \varepsilon_{d,\mu,2} = \left(\frac{\partial a(\theta_d)}{\partial \theta_d} \right)^* \mathbf{d}^H(f_d) \mathbf{\Lambda} |\boldsymbol{\mu}|^2 \in \mathbb{C}, \quad \varepsilon_{K,\mu} = \left(2\pi T_0 \frac{\partial a(\theta_d)}{\partial \theta_d} \right) \mathbf{1}_{K \times 1}^T \mathbf{\Lambda} (\boldsymbol{\varphi} \odot \boldsymbol{\mu}) \in \mathbb{C}, \\
\varepsilon_{d,\mu,1} &= \mathbf{d}^H(f_d) \mathbf{\Lambda} \boldsymbol{\mu} \in \mathbb{C}, \quad \varepsilon_{d,K,\mu} = (2\pi T_0) \mathbf{d}^H(f_d) \mathbf{\Lambda} (\boldsymbol{\varphi} \odot \boldsymbol{\mu}) \in \mathbb{C}. \tag{13}
\end{aligned}$$

$$+ \operatorname{tr} \left\{ \operatorname{diag}^{-1} \{ \boldsymbol{\eta} \} \frac{\partial \operatorname{diag} \{ \boldsymbol{\eta} \}}{\partial [\boldsymbol{\alpha}]_p} \operatorname{diag}^{-1} \{ \boldsymbol{\eta} \} \frac{\partial \operatorname{diag} \{ \boldsymbol{\eta} \}}{\partial [\boldsymbol{\alpha}]_q} \right\}. \tag{9}$$

The second term in (9) denotes the impact of noise. Intuitively, when the SNR is high, the second term becomes small. Thus, by applying Lemma 1, the FIM can be approximately simplified into:

$$\mathbf{F}(\boldsymbol{\alpha}) \approx 2 \operatorname{Re} \left\{ \left(\frac{\partial \boldsymbol{\chi}}{\partial \boldsymbol{\alpha}^T} \right)^H \operatorname{diag}^{-1} \{ \boldsymbol{\eta} \} \frac{\partial \boldsymbol{\chi}}{\partial \boldsymbol{\alpha}^T} \right\}. \tag{10}$$

Based on the definition of $\boldsymbol{\alpha}$ given in (8), the CRB of f_d is the first diagonal element of the inverse matrix of $\mathbf{F}(\boldsymbol{\alpha})$. With the detailed derivations provided in Appendix A, the CRB of f_d is presented below.

Proposition 1. *The closed-form CRB of the Doppler estimation based on the CSI ratio model given in (7) is:*

$$\operatorname{CRB}_{f_d} = [\mathbf{H}^{-1}]_{1,1}, \tag{11}$$

where

$$\mathbf{H} = \frac{2|\xi_d|^2}{\sigma_n^2} \begin{bmatrix} |\rho_2|^2 (\varepsilon_{K,2} - \gamma_{11}) & \operatorname{Im} \{ \rho_2^* \varepsilon_{K,\mu} \} - \gamma_{12} \\ \operatorname{Im} \{ \rho_2^* \varepsilon_{K,\mu} \} - \gamma_{12} & \left| \frac{\partial a(\theta_d)}{\partial \theta_d} \right|^2 \varepsilon_{\mu,2} - \gamma_{22} \end{bmatrix}. \tag{12}$$

The intermediate variables are given in (13) at the top of the next page.

It is not easy to analyze the sensing performance directly from the CRB obtained in (11). However, with proper approximations, some interesting insights can be made. This is illustrated next.

B. Approximated CRB

In this subsection, the approximated CRB is derived to facilitate further analysis of sensing performance. The approximation here is mainly based on the value of Doppler frequency. Intuitively, if the Doppler frequency of the dynamic target is close to 0, the dynamic target signal will be mixed into the static object signal, making the Doppler frequency hard to be estimated. More rigorously, as can be verified by the results in Proposition 1, the CRB for the Doppler frequency approaches infinity as f_d becomes increasingly close to 0. The interference of static path to the dynamic

one can be evaluated by the Doppler pattern, as defined by $\mathcal{P}(\boldsymbol{\varphi}, f_d) = \left| \frac{1}{K} \sum_{k=0}^{K-1} e^{j2\pi \varphi_k T_0 f_d} \right|$. The summation enclosed in $|\cdot|$ can be seen as the signal leakage from the static path to the moving path in the Doppler domain.

Fig. 1 exemplifies two cases of $\mathcal{P}(\boldsymbol{\varphi}, f_d)$, where $K_{\text{all}} = 140$. In particular, Fig. 1 (a) shows the general case with $\varphi_k = k$ and $K = K_{\text{all}}$. Fig. 1 (b) shows a specific case with φ_k given in (20). Note that this φ_k is designed for enhancing sensing performance. With details to be presented later, we focus on illustrating the Doppler pattern here. Despite the oscillation in Fig. 1 (b), the envelope has a similar shape to the Doppler pattern shown in Fig. 1 (a). One can see that the shape of $\mathcal{P}(\boldsymbol{\varphi}, f_d)$ or its envelope has a mainlobe around $f_d T_0 = 0$. The width of the mainlobe basically asserts the range of Doppler values that have poor estimation performance using CSI ratios. To depict the mainlobe region, we introduce the single-sided mainlobe width of the Doppler pattern, as given by $f_{d,M}$, which is defined as:

$$f_{d,M} \approx \max \left\{ \arg \min_{f_d} |\mathcal{P}(\boldsymbol{\varphi}, f_d) - 0.707| \right\}. \tag{14}$$

Note that the above definition has taken into account cases similar to Fig. 1 (b) by using the envelope of the Doppler pattern. We also note that the above definition does not apply to Doppler patterns with grating lobes. This is because through the design of $\boldsymbol{\varphi}$, grating lobes can be readily avoided, which will be further detailed in Section IV.

For convenience of further analysis, we also introduce $R_{\text{SN}} = \frac{(|h_{s,0}|^2 + |h_{s,1}|^2)/2}{\sigma_n^2}$, which denotes the average-static-object power to noise power ratio, $R_{\text{SD}} = \frac{(|h_{s,0}|^2 + |h_{s,1}|^2)/2}{|\xi_d|^2}$, which denotes the average-static-object power to dynamic-target power ratio, and $R_A = \frac{|h_{s,1} - a(\theta_d) h_{s,0}|^2}{|h_{s,0}|^2 + |h_{s,1}|^2}$. By expanding the numerator of R_A , we can obtain $R_A = 1 - \frac{2 \operatorname{Re} \{ a(\theta_d) h_{s,0} h_{s,1}^* \}}{|h_{s,0}|^2 + |h_{s,1}|^2}$. Thus, R_A can partially reflect the impact of the angular difference between the dynamic and static paths. Moreover, under all possible θ_d , we further have:

$$0 \leq \frac{(|h_{s,0}| - |h_{s,1}|)^2}{|h_{s,0}|^2 + |h_{s,1}|^2} \leq R_A \leq \frac{(|h_{s,0}| + |h_{s,1}|)^2}{|h_{s,0}|^2 + |h_{s,1}|^2} \leq 2. \tag{15}$$

Now, we are ready to introduce the following CRB approximation.

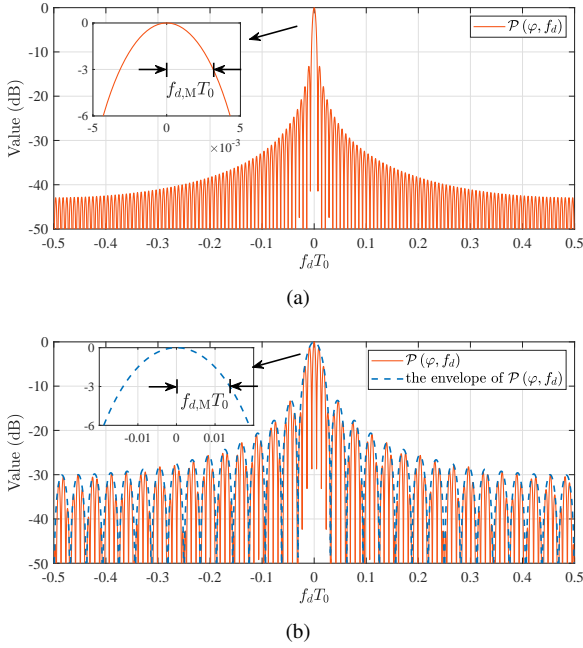


Fig. 1. The definition of the mainlobe, exemplifying two cases. (a) $K_{\text{all}} = K = 140$, and $\varphi_k = k$. (b) $K_{\text{all}} = 140$, $K = 64$, and φ_k follows (20).

Proposition 2. When $|f_d| > f_{d,M}$, and $R_{SD} \rightarrow 0$ or $R_{SD} \rightarrow +\infty$, the Doppler CRB can be approximated by:

$$CRB_{f_d} \approx \frac{1}{8\pi^2 T_0^2 K} \frac{1}{S_{\varphi,2} - S_{\varphi,1}^2} \frac{\sqrt{(1 - R_{SD})^2 + 2R_A R_{SD}}}{R_{SN} R_A}, \quad (16)$$

where $S_{\varphi,1} = \frac{1}{K} \mathbf{1}_{K \times 1}^T \boldsymbol{\varphi}$; $S_{\varphi,2} = \frac{1}{K} \boldsymbol{\varphi}^T \boldsymbol{\varphi}$; and $\boldsymbol{\varphi} = [\varphi_0, \dots, \varphi_{K-1}]^T \in \mathbb{Z}^{K \times 1}$.

Proof. Please refer to Appendix B. Note that the relationship between $f_{d,M}$ and CRB is also established in Appendix B. \square

Note that we can relax the conditions “ $R_{SD} \rightarrow 0$ or $R_{SD} \rightarrow +\infty$ ” to “ $R_{SD} < 0.1$ or $R_{SD} > 8$ ” based on (36) in Appendix B. The approximated CRB has a clearer structure, compared with the original one in Proposition 1, which can be exploited for further investigating the impact of different physical quantities on the Doppler estimation. This is detailed next.

C. Insights Drawn From the Approximated CRB

In this subsection, some interesting properties of CRB_{f_d} are unveiled, highlighting the impact of different factors on the CSI ratio-based Doppler estimation.

We start with R_A by presenting the following result.

Corollary 1. CRB_{f_d} is a monotonically decreasing function of R_A .

Proof. The partial derivative of CRB_{f_d} with respect to R_A is given by:

$$\frac{\partial CRB_{f_d}}{\partial R_A} \propto \frac{-(1 - R_{SD})^2 - R_{SD} R_A}{R_{SN} R_A^2 \sqrt{(1 - R_{SD})^2 + 2R_A R_{SD}}}. \quad (17)$$

Given the inequality in (15), (17) is always smaller than zero. A more accurate Doppler estimation can be obtained by enhancing R_A . Corollary 1 is thus proved. \square

As mentioned earlier, R_A is closely related with the dynamic target angle θ_d , which, hence, suggests that the CRB of Doppler estimation varies with the AoA of the dynamic path. An interesting question follows: how sensitive the CRB can be against θ_d ? To investigate this, let us check the ratio of the maximum and minimum values of the CRB in $\theta_d \in [-\frac{\pi}{2}, \frac{\pi}{2}]$, i.e., $\frac{\max_{\theta_d} CRB}{\min_{\theta_d} CRB}$. A small value of $\frac{\max_{\theta_d} CRB}{\min_{\theta_d} CRB}$ illustrates that the CRB is not sensitive to the dynamic target angle. Specifically, some interesting results are provided below.

Corollary 2. The following three relationships hold:

$$\arg \min_{\sin \theta_d} CRB \approx \frac{\lambda}{2\pi d} \angle \{h_{s,1}/h_{s,0}\} + \frac{\lambda}{d} \left(\frac{1}{2} - z_I \right), \quad (18a)$$

$$\arg \max_{\sin \theta_d} CRB \approx \frac{\lambda}{2\pi d} \angle \{h_{s,1}/h_{s,0}\} - \frac{z_A \lambda}{d}, \quad (18b)$$

$$\frac{\max_{\theta_d} CRB}{\min_{\theta_d} CRB} \approx \frac{(|h_{s,1}| + |h_{s,0}|)^2}{(|h_{s,1}| - |h_{s,0}|)^2}. \quad (18c)$$

where the value of $z_I, z_A \in \mathbb{Z}$ can ensure the value on the right side of (18a) and (18b) within $(-1, 1)$, respectively.

Proof. Using (18b) as an example. Based on Corollary 1, a maximal CRB can be achieved when R_A is minimal, which means $R_A = \frac{(|h_{s,0}| - |h_{s,1}|)^2}{|h_{s,0}|^2 + |h_{s,1}|^2}$, and we have $\text{Re} \left\{ a(\theta_d) \frac{h_{s,0}}{|h_{s,0}|} \frac{h_{s,1}^*}{|h_{s,1}|} \right\} = 1$. Due to $a(\theta_d) = e^{j \frac{2\pi}{\lambda} d \sin \theta_d}$, the equation $\sin \theta_d = \frac{\lambda}{2\pi d} \angle \{h_{s,1}/h_{s,0}\}$ holds when CRB reaches its maximum. Note that the value of $\sin \theta_d$ ranges from -1 to 1 . The term $\frac{z_A \lambda}{d}$ is thus required. The results in (18a) and (18c) can be proved similarly. \square

From Corollary 2, we see that $|h_{s,0}|$ should not equal to $|h_{s,1}|$; otherwise the CRB approaches infinite, suggesting that the CSI ratio cannot be used for Doppler sensing. Moreover, we also see from Corollary 2 that the dynamic target angle has negligible impact on the CRB when $|h_{s,1}/h_{s,0}| \ll 1$ or $|h_{s,1}/h_{s,0}| \gg 1$ due to $\frac{\max_{\theta_d} \sqrt{CRB}}{\min_{\theta_d} \sqrt{CRB}} \approx 1$.

Remark 1. If $|h_{s,0}| \approx |h_{s,1}|$, we can then combine all static objects in space into one equivalent static object with angle $\bar{\theta}_s = \arcsin \left\{ \frac{\lambda}{2\pi d} \angle \{h_{s,1}/h_{s,0}\} \right\}$. The CSI ratio can generate estimates with large errors when the angles of the dynamic target and the equivalent static objects are close. This is consistent with what is observed from Corollary 2. In most cases, this result does not occur simultaneously across all subcarriers. We can always find subcarriers that yield relative accurate estimates.

Depending on whether the static path’s power is dominant, or not, compared with the dynamic path’s power, we can further simplify the CRB, as follows.

Corollary 3. If $R_{SD} \gg 1$ (e.g., the presence of LOS path),

$$CRB_{f_d} \approx \left[8\pi^2 T_0^2 K (S_{\varphi,2} - S_{\varphi,1}^2) \right]^{-1} \frac{R_{SD}}{R_{SN} R_A}$$

$$= [8\pi^2 T_0^2 K (S_{\varphi,2} - S_{\varphi,1}^2)]^{-1} \frac{1}{R_A} \frac{\sigma_n^2}{|\xi_d|^2}, \quad (19a)$$

which is inversely proportional to $|\xi_d|^2$. In contrast, if $R_{SD} \ll 1$,

$$\begin{aligned} \text{CRB}_{f_d} &\approx [8\pi^2 T_0^2 K (S_{\varphi,2} - S_{\varphi,1}^2)]^{-1} \frac{1}{R_{SN} R_A} \\ &= [8\pi^2 T_0^2 K (S_{\varphi,2} - S_{\varphi,1}^2)]^{-1} \frac{2\sigma_n^2}{|h_{s,1} - a(\theta_d) h_{s,0}|^2}, \end{aligned} \quad (19b)$$

which is independent of R_{SD} .

Proof. Defining $\mathcal{L}_{R_{SD}} = \sqrt{(1 - R_{SD})^2 + 2R_A R_{SD}}$ based on (16), the Doppler CRB in (16) is inversely proportional to $\mathcal{L}_{R_{SD}}$. We now evaluate $\mathcal{L}_{R_{SD}}$ with respect to R_{SD} .

In Case A, we have $R_{SD} \gg 1$, and $\mathcal{L}_{R_{SD}} \approx R_{SD}$. The term R_{SN} in the numerator of (16) is combined with R_{SD} , making the CRB inversely proportional to $|\xi_d|^2$. In Case B, we have $R_{SD} \ll 1$, and $\mathcal{L}_{R_{SD}} \approx 1$, which is unrelated with R_{SD} . Corollary 3 is thus proved. \square

The insights unveiled in this section are helpful in the waveform design for enhancing sensing performance. This is performed next.

IV. OPTIMIZATION FOR OFDM SYMBOLS

Utilizing the derived CRB and analysis made above, we proceed to optimize the OFDM symbol index φ_k ($0 \leq \varphi_k \leq K_{\text{all}} - 1$, $k = 0, \dots, K - 1$) to improve the Doppler sensing performance using CSI ratios. Recall that we use $\varphi = [\varphi_0, \dots, \varphi_{K-1}]^T \in \mathbb{Z}^{K \times 1}$ to collect indexes of K out of K_{all} OFDM symbols used for sensing.

A. Strategy of Optimizing φ

Based on Section III-B, a low CRB can be achieved by optimizing two terms, which are $\mathcal{L}_1(\varphi) = S_{\varphi,2} - S_{\varphi,1}^2$ (unrelated with f_d) and the Doppler pattern $\mathcal{P}(\varphi, f_d) = \left| \frac{1}{K} \sum_{k=0}^{K-1} e^{j2\pi\varphi_k T_0 f_d} \right|$ (related with f_d and defined in Section III-B). These further lead to the following metrics.

- Value of $\mathcal{L}_1(\varphi)$: The value of $\mathcal{L}_1(\varphi)$ has significant impact on CRB. As indicated by (16), CRB_{f_d} is inversely proportional to $\mathcal{L}_1(\varphi)$. The term φ_k should be selected by maximizing $\mathcal{L}_1(\varphi)$;
- Mainlobe width of $\mathcal{P}(\varphi, f_d)$: The mainlobe width of $\mathcal{P}(\varphi, f_d)$ (i.e., $f_{d,M}$ defined in Section III-B) should be as narrow as possible. As aforementioned in Section III-B, the CRB will sharply increase when f_d is close to the mainlobe of CRB. In some scenarios, such as indoor localization and vital sign detection, where the Doppler of the dynamic target is usually low, a narrow mainlobe (i.e., a small $f_{d,M}$) is able to improve the estimation accuracy;
- Sidelobe of $\mathcal{P}(\varphi, f_d)$: The sidelobe of $\mathcal{P}(\varphi, f_d)$ causes the fluctuation of the CRB under different f_d values, which can render large CRB values at some Doppler frequencies. Thus, reducing sidelobes and ensuring uniformness in a Doppler frequency region of interest can help ensure a high and uniform sensing performance.

Based on the above analysis, our strategy of optimizing φ is given as: *the optimization should maximize the value of*

$\mathcal{L}_1(\varphi)$ and minimize the mainlobe width ($f_{d,M}$) while keeping the sidelobe of $\mathcal{P}(\varphi, f_d)$ minimal.

Note that these performance metrics play critical roles in different sensing scenarios. In particular, when static paths are strong and the Doppler frequency of the dynamic path is small, the dynamic path is more likely to be severely interfered by the static paths. This scenario is interference-limited, where more focus can be placed on reducing the mainlobe width of $\mathcal{P}(\varphi, f_d)$. In contrast, when the Doppler frequency of the dynamic path is far from zero with little interference from static paths, its estimation performance is mainly determined by noises, i.e., a noise-limited case. In such a case, CRB intrinsically asserts the estimation performance, and hence $\mathcal{L}_1(\varphi)$ can be mainly adopted for waveform design. Next, we illustrate the CRB-driven waveform designs in these two cases.

B. Noise-limited Waveform Design

Consider noise-limited cases first. We can then focus on $\mathcal{L}_1(\varphi)$ only, as $\mathcal{P}(\varphi, f_d)$ mainly asserts the mutual interference between static and dynamic paths.

In such cases, the optimal OFDM symbol index can be obtained by maximizing $\mathcal{L}_1(\varphi)$. With the CRB results in Proposition 2, one can validate the following result. The details are suppressed here for conciseness.

Proposition 3. (Noise-limited Doppler Sensing) For $0 \leq \varphi_k \leq K_{\text{all}} - 1$ and $k = 0, \dots, K - 1$, the OFDM symbol φ_k indexes collected by the following vector maximizes $\mathcal{L}_1(\varphi)$:

$$\varphi_{\text{op}}^{\text{gen}} = \left[\kappa_{K/2,A}^T, (K_{\text{all}} - 1) \mathbf{1}_{K/2 \times 1}^T - \kappa_{K/2,B}^T \right]^T, \quad (20)$$

where $\kappa_{K/2,A} = \kappa_{K/2,B} = [0, 1, \dots, \lfloor K/2 \rfloor - 1]^T \in \mathbb{Z}^{\lfloor K/2 \rfloor \times 1}$ if K is even. If K is odd, $\kappa_{K/2,A} = [0, 1, \dots, \lfloor K/2 \rfloor - 1]^T \in \mathbb{Z}^{\lfloor K/2 \rfloor \times 1}$ and $\kappa_{K/2,B} = [0, 1, \dots, \lfloor K/2 \rfloor - 1]^T$, or $\kappa_{K/2,A} = [0, 1, \dots, \lfloor K/2 \rfloor - 1]^T$ and $\kappa_{K/2,B} = [0, 1, \dots, \lfloor K/2 \rfloor - 1]^T$.

Proposition 3 suggests that, to optimize the theoretical Doppler sensing performance using CSI ratios in noise-limited cases, the OFDM symbols should be selected *near the two ends of the available OFDM symbols*. Moreover, the symbol indexes are symmetrical to the center and occupy the maximum observation time of the available symbols. Additionally, the symmetry pattern in $\varphi_{\text{op}}^{\text{gen}}$ results in a nice feature of the Doppler pattern. The feature can be used for further simplifying the waveform design; please refer to Appendix D for its proof.

Proposition 4. If the indexes of the OFDM symbols used for sensing are symmetric against the point $(K_{\text{all}} - 1)/2$, i.e., φ has a structure of $\varphi = [\tilde{\varphi}^T, K_{\text{all}} - 1 - \tilde{\varphi}^T]^T$, where $\tilde{\varphi} \in \mathbb{Z}^{K/2 \times 1}$, the envelope of $\mathcal{P}(\varphi, f_d)$ is solely determined by half indexes and can be given by:

$$\mathcal{E}_{\mathcal{P}}(\tilde{\varphi}, f_d) = \left| \frac{2}{K} \sum_{k=0}^{\frac{K}{2}-1} e^{j2\pi[\tilde{\varphi}]_k T_0 f_d} \right|. \quad (21)$$

Employing Proposition 4, the envelope of $\mathcal{P}(\varphi_{\text{op}}^{\text{gen}}, f_d)$ is $\mathcal{E}_{\mathcal{P}}(\tilde{\varphi}_{\text{op}}^{\text{gen}}, f_d) = \left| \frac{\text{sinc}(\frac{K}{2} T_0 f_d)}{\text{sinc}(T_0 f_d)} \right|$ whose mainlobe width is related

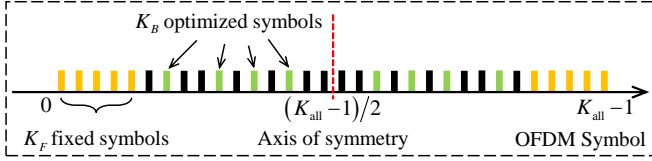


Fig. 2. Illustration of the structure of φ in optimization algorithm, with $K_{\text{all}} = 32$, $K = 18$, $K_F = 5$, and $K_B = 4$, where $K_F + K_B = K/2$.

with $K/2$ instead of K_{all} . In Fig. 1 (b), we plot $\mathcal{P}(\varphi_{\text{op}}^{\text{gen}}, f_d)$ and its envelope $\mathcal{E}_{\mathcal{P}}(\varphi_{\text{op}}^{\text{gen}}, f_d)$ based on Proposition 3 and Proposition 4. It can be seen that $\mathcal{P}(\varphi_{\text{op}}^{\text{gen}}, f_d)$ is modulated by a “high-frequency oscillating signal”, which is essentially caused by the signal in (43). In such cases, the envelope $\mathcal{E}_{\mathcal{P}}(\varphi_{\text{op}}^{\text{gen}}, f_d)$ plays a critical role in the Doppler sensing performance rather than $\mathcal{P}(\varphi_{\text{op}}^{\text{gen}}, f_d)$.

As illustrated in Section III, the mainlobe of the Doppler pattern or its envelope asserts the strong interference between static and dynamic paths. A wide mainlobe or high sidelobes can degrade Doppler sensing performance. Next, we show that designing the sensing symbol indexes in φ can help minimize mainlobe width and sidelobe levels in a Doppler pattern.

C. Interference-limited Waveform Design

In this subsection, we optimize φ_k to reduce the mainlobe width and the sidelobe level of $\mathcal{E}_{\mathcal{P}}(\tilde{\varphi}, f_d)$ for better sensing performance. For ease of illustration, we focus on the case of even K .

Proposition 3 indicates that the maximal $\mathcal{L}_1(\varphi)$ is obtained when φ_k is symmetrically located near the two ends of all available symbols. Now, we need to release this constraint in exchange of the reduced mainlobe and sidelobe of Doppler pattern. We introduce the structure of φ , as depicted in Fig. 2, to factor in the trade-off between optimizing $\mathcal{L}_1(\varphi)$ and $\mathcal{P}(\varphi, f_d)$. Specifically, we fix $2K_F$ OFDM symbols near the two ends of $\varphi_{\text{op}}^{\text{gen}}$ as given in (20) and allow the remaining $2K_B$ OFDM symbols to be reconfigured for optimizing $\mathcal{P}(\varphi, f_d)$. Since $K_F + K_B = K/2$, the value of K_B controls the trade off between the two objectives. In an extreme case of $K_B = K/2$, the complete focus is placed on reducing the interference between static and dynamic paths.

Based on Fig. 2, $\tilde{\varphi}$ can be further rewritten as $\tilde{\varphi} = [\tilde{\varphi}_F^T, \tilde{\varphi}_B^T]^T \in \mathbb{Z}^{K/2 \times 1}$, where $\tilde{\varphi}_F = [0, 1, \dots, K_F - 1]^T \in \mathbb{Z}^{K_F \times 1}$, $\tilde{\varphi}_B \in \mathbb{Z}^{K_B \times 1}$. This leaves $\tilde{\varphi}_B$ for optimization next.

Since $\tilde{\varphi}_B$ is an integer vector, it can be solved via an integer optimization problem, which is generally challenging to solve. Fortunately, we have the following result to substantially simplify the task of optimizing $\tilde{\varphi}_B$.

Proposition 5. For $\tilde{\varphi}'_B = \tilde{\varphi}_B + \delta_B$, where each entry of δ_B is continuous in $(-0.5, 0.5)$, and hence, $\tilde{\varphi}_B = \text{round}\{\tilde{\varphi}'_B\}$, we have:

$$\left| \mathcal{E}_{\mathcal{P}}\left(\begin{bmatrix} \tilde{\varphi}_F \\ \tilde{\varphi}_B \end{bmatrix}, f_d\right) - \mathcal{E}_{\mathcal{P}}\left(\begin{bmatrix} \tilde{\varphi}_F \\ \tilde{\varphi}'_B \end{bmatrix}, f_d\right) \right| < \frac{\pi K_B}{K/2} |T_0 f_d|, \quad (22)$$

where $|T_0 f_d| \leq T_0 f_{d,M}$.

Proof. Please refer to Appendix E. \square

We note that the right-hand side of (22) is generally smaller than $\pi/30$. As seen from Fig. 1, $|T_0 f_d| \leq T_0 f_{d,M} < 1/30$. Note that Fig. 1 (b) actually illustrates the maximum mainlobe width. The vector φ used for plotting the figure is obtained by maximizing $\mathcal{L}_1(\varphi)$ in Proposition 3 without considering the Doppler pattern. To further validate this, let us check a numerical example. For instance, considering $\varphi_{\text{op}}^{\text{gen}}$ defined in (20), its mainlobe width can be calculated as $T_0 f_{d,M} \approx \frac{0.44}{K/2}$. When $K = 128$ and $K_B = 50$, (22) is lower than 1.69×10^{-2} .

Proposition 5 suggests that the rounding operation has negligible impact on $\mathcal{E}_{\mathcal{P}}(\tilde{\varphi}, f_d)$'s mainlobe. This enables us to conveniently solve a non-integer optimization problem for optimizing continuous $\tilde{\varphi}'_B$ and then rounding it element-wise to obtain $\tilde{\varphi}_B$.

It is obvious that simultaneously minimizing the mainlobe width and sidelobe level of patterns shown in Fig. 1 are contradicting objectives. Thus, we choose to minimize the sidelobe level, subject to an upper bound of the mainlobe width, as denoted by $f_{d,M}^{\text{ex}}$. For the sidelobe suppression, we adopt the weighted sidelobe power \mathcal{P}_{SL} , as given by:

$$\mathcal{P}_{\text{SL}} = \int_{f_{d,M}^{\text{ex}}}^{\frac{1}{2T_0}} \varpi(f_d) |\mathcal{E}_{\mathcal{P}}(\tilde{\varphi}, f_d)|^2 df_d, \quad (23)$$

where $\varpi(f_d)$ denotes the weighted function with respect to f_d . Note that $\varpi(f_d)$ controls the proportion of $\mathcal{E}_{\mathcal{P}}(\tilde{\varphi}, f_d)$ on different f_d in \mathcal{P}_{SL} . We can formulate the following optimization problem to achieve the strategy illustrated in Section IV-A:

$$\begin{aligned} & \min_{\tilde{\varphi}_B} \mathcal{P}_{\text{SL}} \\ & \text{s.t. } \mathbf{1}_{K_B \times 1} K_F \leq \tilde{\varphi}_B \leq \mathbf{1}_{K_B \times 1} \left\lceil \frac{K_{\text{all}} - 1}{2} \right\rceil \\ & f_{d,M}^{\text{ex}} \leq |f_d| \leq \frac{1}{2T_0} \\ & \varphi = [\tilde{\varphi}_F^T, K_{\text{all}} - 1 - \tilde{\varphi}_B^T]^T \\ & \tilde{\varphi} = [\tilde{\varphi}_F^T, \tilde{\varphi}_B^T]^T. \end{aligned} \quad (24)$$

Inspired by [27], we introduce a perturbation on $\tilde{\varphi}_B$ and iteratively optimize the perturbation to minimize the objective function in (23). The vector updated in the $(i+1)$ step is expressed as:

$$\tilde{\varphi}_B^{(i+1)} = \tilde{\varphi}_B^{(i)} + \Delta \tilde{\varphi}_B^{(i+1)}, \quad (25)$$

where $\Delta \tilde{\varphi}_B^{(i+1)} \in \mathbb{R}^{K_B \times 1}$ denotes a perturbation amount for $\tilde{\varphi}_B^{(i)}$. Note that the value range of each element in $\tilde{\varphi}_B$ is from K_F to $\lceil \frac{K_{\text{all}} - 1}{2} \rceil - 1$. We consider the elements of the initialization vector $\tilde{\varphi}_B^{(0)}$ distributed at equal intervals in the above range. This ensures that the sidelobes nearby the mainlobe have relatively small values. The i -th element of $\tilde{\varphi}_B^{(0)}$ is thus given by:

$$[\tilde{\varphi}_B^{(0)}]_i = K_F + \text{round} \left\{ i \frac{\lceil \frac{K_{\text{all}} - 1}{2} \rceil - 1 - K_F}{K_B - 1} \right\}, \quad (26)$$

where $i = 0, \dots, K_B - 1$.

Assume that the value of $\Delta\tilde{\varphi}_B^{(i+1)}$ is small, $\mathcal{E}_{\mathcal{P}}(\tilde{\varphi}, f_d)$, as given in (21), can be approximated by:

$$\begin{aligned} \mathcal{E}_{\mathcal{P}}(\tilde{\varphi}, f_d) &= \frac{2}{K} \left| \sum_{k=0}^{K_F-1} e^{j2\pi[\tilde{\varphi}_F]_k T_0 f_d} + \sum_{k=0}^{K_B-1} e^{j2\pi[\tilde{\varphi}_B^{(i)} + \Delta\tilde{\varphi}_B^{(i+1)}]_k T_0 f_d} \right| \\ &= \frac{2}{K} \left| \mathbf{f}^T(\tilde{\varphi}_F, f_d) \mathbf{1}_{K_F \times 1} + \mathbf{f}^T(\tilde{\varphi}_B^{(i)}, f_d) \mathbf{f}(\Delta\tilde{\varphi}_B^{(i+1)}, f_d) \right| \\ &\approx \frac{2}{K} \left| \mathbf{f}^T(\tilde{\varphi}, f_d) \mathbf{1}_{K/2 \times 1} + j2\pi T_0 f_d \mathbf{f}^T(\tilde{\varphi}_B^{(i)}, f_d) \Delta\tilde{\varphi}_B^{(i+1)} \right|, \end{aligned} \quad (27)$$

where $\mathbf{f}(\tilde{\varphi}, f_d) \triangleq e^{j2\pi\tilde{\varphi}T_0 f_d}$.

This enables the optimization problem (24) to be converted into minimizing the following function in terms of $\Delta\tilde{\varphi}_B$:

$$\mathcal{H}_{\text{op}}^{(i+1)} = \mathcal{P}_{\text{SL}}^{(i+1)} + a \left(\mathbf{w}^{(i)} \right)^T \left(\Delta\tilde{\varphi}_B^{(i+1)} \right)^2, \quad (28)$$

where $a \in \mathbb{R}^+$ is a weight, which controls the convergence rate. Moreover, $\mathbf{w}^{(i)} = [w_0^{(i)}, \dots, w_{K_B-1}^{(i)}]^T \in \mathbb{R}^{K_B \times 1}$ is a weighting vector restricting the value range of $\tilde{\varphi}_B^{(i)}$, where $w_{k_B}^{(i)} = 1$ if $K_F + 1 < [\tilde{\varphi}_B^{(i)}]_{k_B} < \lfloor \frac{K_{\text{all}}-1}{2} \rfloor - 1$, and $w_{k_B}^{(i)} = \inf$ if $[\tilde{\varphi}_B^{(i)}]_{k_B} \leq K_F + 1$ or $[\tilde{\varphi}_B^{(i)}]_{k_B} \geq \lfloor \frac{K_{\text{all}}-1}{2} \rfloor - 1$. Note that the second term in (28) is subject to the fact that each element in $\Delta\tilde{\varphi}_B^{(i+1)}$ has a small value.

As derived in Appendix F, the updated vector $\Delta\tilde{\varphi}_B^{(i+1)}$ can be solved as:

$$\Delta\tilde{\varphi}_B^{(i+1)} = \left(\text{Re} \left\{ \mathbf{V}_2^{(i)} \right\} + a \text{diag} \left\{ \mathbf{w}^{(i)} \right\} \right)^{-1} \text{Im} \left\{ \mathbf{V}_1^{(i)} \right\} \mathbf{1}_{\frac{K}{2} \times 1}, \quad (29)$$

where $\mathbf{V}_1^{(i)} = \frac{8\pi T_0}{K^2} \int_{f_{d,M}^{\text{ex}}}^{\frac{1}{2T_0}} \varpi(f_d) f_d \mathbf{f}(\tilde{\varphi}_B^{(i)}, f_d) \mathbf{f}^H(\tilde{\varphi}, f_d) df_d$, $\mathbf{V}_2^{(i)} = \frac{4(2\pi T_0)^2}{K^2} \int_{f_{d,M}^{\text{ex}}}^{\frac{1}{2T_0}} \varpi(f_d) f_d^2 \mathbf{f}(\tilde{\varphi}_B^{(i)}, f_d) \mathbf{f}^H(\tilde{\varphi}_B^{(i)}, f_d) df_d$, and $\mathbf{V}_1^{(i)} \in \mathbb{C}^{K_B \times \frac{K}{2}}$, $\mathbf{V}_2^{(i)} \in \mathbb{C}^{K_B \times K_B}$. When $|\Delta\tilde{\varphi}_B^{(i+1)} - \Delta\tilde{\varphi}_B^{(i)}|$ is lower than a preset threshold, the iteration converges and we obtain $\tilde{\varphi}_B^{(I)}$ and then take the rounding of $\tilde{\varphi}_B^{(I)}$ as the optimized $\tilde{\varphi}_B$:

$$\tilde{\varphi}_B^{\text{op}} = \text{round} \left\{ \tilde{\varphi}_B^{(I)} \right\}. \quad (30)$$

Finally, we construct the optimal φ :

$$\varphi^{\text{op}} = \left[\tilde{\varphi}_F^T, (\tilde{\varphi}_B^{\text{op}})^T, K_{\text{all}}-1-\tilde{\varphi}_F^T, K_{\text{all}}-1-(\tilde{\varphi}_B^{\text{op}})^T \right]^T. \quad (31)$$

Algorithm 1 summarizes the proposed waveform design for the interference-limited Doppler sensing using CSI ratios.

V. SIMULATION RESULTS

In this section, simulation results are presented to validate the preceding CRB derivations, analysis and waveform design. The carrier frequency is set to 3GHz, so the wavelength is $\lambda = 0.1\text{m}$. Suppose that the CSI-ratio model utilizes two received antennas with the spacing $d = \lambda/2 = 0.05\text{m}$. The time interval between OFDM symbols is $T_0 = 125\mu\text{s}$, so the range of unambiguous Doppler is $|f_d| \leq \frac{1}{2T_0} = 4000\text{Hz}$,

Algorithm 1 Proposed Waveform Design for Interference-Limited Doppler Sensing

Input: the number of the available OFDM symbols K_{all} , the number of the symbols allocated for sensing K , the number of the fixed symbols K_F , the expected mainlobe width $f_{d,M}^{\text{ex}}$, the symbol interval T_0 , and the weighting function $\varpi(f_d)$.

Output: the optimal OFDM symbol vector φ^{op} .

- 1: Constructing $\tilde{\varphi}_F = [0, 1, \dots, K_F - 1]^T \in \mathbb{Z}^{K_F \times 1}$ and calculating $K_B = K/2 - K_F$.
- 2: **Initialize:** Performing (26) and $i = 0$.
- 3: **while** $\Delta\tilde{\varphi}_B^{(i+1)} - \Delta\tilde{\varphi}_B^{(i)} > \text{threshold}$ **do**
- 4: Updating $\mathbf{w}^{(i)}$ by $\tilde{\varphi}_B^{(i)}$ and calculating $\mathbf{V}_1^{(i)}$ and $\mathbf{V}_2^{(i)}$.
- 5: Calculate $\Delta\tilde{\varphi}_B^{(i+1)}$ by (29) and updating $\tilde{\varphi}_B^{(i+1)}$ by (25).
- 6: **end while**
- 7: Performing (30) and (31) for φ^{op} .

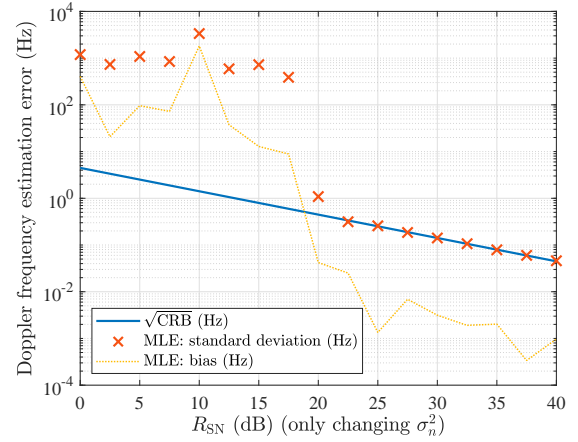


Fig. 3. Doppler CRBs (11) and the MLE results versus R_{SN} .

i.e., $|v| \leq \frac{\lambda}{4T_0} = 200\text{m/s}$. Unless otherwise specified, we set the number of the allocated OFDM symbols used for uplink sensing to $K = 128$ and the set the available number of OFDM symbols to $K_{\text{all}} = 512$. The OFDM symbol index follows the noise-limited Doppler sensing method given in (20).

The radial velocity of the dynamic target is set to 5m/s, so the Doppler frequency is $f_d = 100\text{Hz}$, and the angle of the dynamic target is $\theta_d = 10^\circ$. We set $\rho_0 = \frac{h_{s,1}}{h_{s,0}} = 1.2e^{-j\frac{30\pi}{180}}$, and $\rho_1 = \frac{\xi_d}{h_{s,0}} = 0.1e^{-j\frac{110\pi}{180}}$. Therefore, we have $R_{\text{SD}} = 122$ (i.e., 20.86dB) and $R_A = 0.527$. To meet the high-SNR requirement given in Lemma 1, a small value of the noise power is required and we set $R_{\text{SN}} = 1220$ (i.e., 30.86dB).

A. Evaluation of the CRB

In this subsection, the simulation and theoretical results are provided for evaluating the CRB.

Fig. 3 presents the CRB and the estimation results using the maximum likelihood estimation (MLE) algorithm with respect to σ_n^2 . Note that only σ_n^2 is changed and the other parameters remain constant in Fig. 3. The MLE algorithm is designed based on the approximation in (4). It can be seen from Fig. 3 that the estimator can be regarded as “unbiased”, in the sense

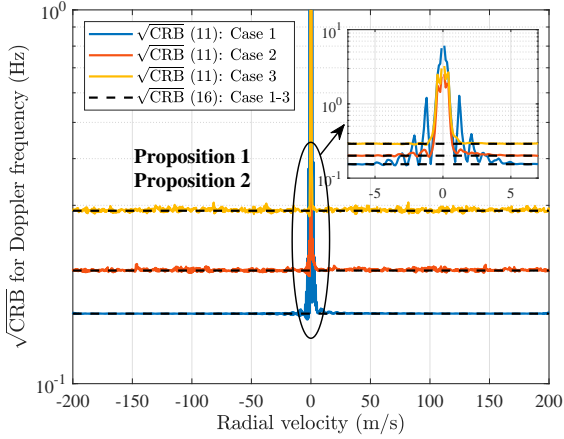


Fig. 4. Doppler CRBs and the MLE results versus radial velocity, comparing CRB results in (11) and (16).

that the bias is negligibly small in high SNR regions, and is basically overlapping with the CRB when $R_{SN} > 22.5\text{dB}$. This verifies the preciseness of the derived CRB in Proposition 2.

Fig. 4 plots the CRBs of three different cases of $\varphi \in \mathbb{Z}^{K \times 1}$ using (11) and (16), respectively. The OFDM symbol index φ of Case 1 follows (20), while φ 's in Cases 2 and 3 are randomly generated. From Fig. 4, we see that Case 1 leads to the minimal CRB in sidelobe regions, which validate Proposition 3. We also see that the actual CRB in (11) and the approximated one in (16) are basically overlapping in sidelobe regions with $|f_d| > f_{d,M}$, which validates the feasibility of using the CRB approximation (16) for the CRB analysis.

Fig. 5 demonstrates the influence of θ_d on Doppler CRBs. Fig. 5 (a) shows the CRB (given by (11)), MLE, and R_A results versus the angle of the dynamic target θ_d . As illustrated in Corollary 1, the Doppler CRB is strongly related with R_A . In Fig. 5 (a), R_A achieves its lowest value when CRB is maximum, which verifies the result in Corollary 1. In addition, the peak position is closely related to the phase of $h_{s,0}$ and $h_{s,1}$. The angle corresponding to the CRB peak can be calculated from the numerator of R_A (i.e., $|h_{s,1} - a(\theta_d)h_{s,0}|^2$), which is $\theta_d = -9.6^\circ$. This is also validated in Fig. 5 (a). Moreover, we see the obvious impact of θ_d on CRB. The ratio of the peak and minimum values of the CRB in Fig. 5 (a) approximately equals to 11, i.e., $\frac{\max_{\theta_d} \sqrt{\text{CRB}}}{\min_{\theta_d} \sqrt{\text{CRB}}} \approx 11$, showing the angle-dependent impact of the equivalent static path on the dynamic path's Doppler estimation in CSI ratio-based sensing.

Fig. 5 (b) further observes the ratio of the maximum and minimum values of the CRB in $\theta_d \in [-\frac{\pi}{2}, \frac{\pi}{2}]$ (i.e., $\frac{\max_{\theta_d} \sqrt{\text{CRB}}}{\min_{\theta_d} \sqrt{\text{CRB}}}$ defined in Corollary 2) to evaluate the variation in CRB values against $|h_{s,1}/h_{s,0}|$. It can be seen that the derivation result in Corollary 2 fits well with the simulation result using (11). From Fig. 5 (b), we know that θ_d has negligible influence on the CRB when $|h_{s,1}/h_{s,0}| \ll 1$ or $|h_{s,1}/h_{s,0}| \gg 1$ due to $\frac{\max_{\theta_d} \sqrt{\text{CRB}}}{\min_{\theta_d} \sqrt{\text{CRB}}} \approx 1$. When the value of $|h_{s,0}|$ is closer to $|h_{s,1}|$, the CRB is more sensitive to the changes on θ_d . An extreme case is $|h_{s,0}| = |h_{s,1}|$, where the ratio value is infinite.

Fig. 5 (c) displays the CRB results when $|h_{s,1}/h_{s,0}| = 1$

under two different cases. Clearly, there is one dynamic target angle that cannot be sensed using CSI ratios. Refer to the angle as the unobservable angle. The angle is strongly dependent of the phase of $h_{s,1}/h_{s,0}$, as can be seen in Fig. 5 (c) and verified from (18b) in Corollary 2. Moreover, each CRB curve in Fig. 5 (c) also has a minimum value. For both curves in Fig. 5 (c), the difference of $\sin(\theta_d)$ corresponding to the maximum and minimum points of the curve equals to $\lambda/2d = 1$, which can be verified from (18a) and (18b). Intuitively, if the angle of the dynamic target deviates further from the unobservable angle, the CRB can be lower.

Fig. 6 shows the CRB and the Doppler estimation, where we only change the value of $|\xi_d|^2$ to observe different R_{SD} . When R_{SD} is sufficiently large, i.e., the dynamic target power $|\xi_d|^2$ is significantly lower than the averaged static object power $(|h_{s,0}|^2 + |h_{s,1}|^2)/2$, a larger $|\xi_d|^2$ brings a more accurate estimation, as shown in Fig. 6. This result can be verified using (19a) in Corollary 3.

B. Evaluation of the CRB Optimization

Next, we evaluate the proposed noise-limited Doppler sensing method in Proposition 3 and the proposed interference-limited Doppler sensing method in Algorithm 1.

Fig. 7 shows the CRB of the proposed noise-limited Doppler sensing method in Proposition 3 under different K/K_{all} . These results are the minimum values that the CRB can achieve with given K/K_{all} and K_{all} when $|f_d| > f_{d,M}$. As can be seen, the CRBs decrease rapidly when K/K_{all} is small. However, when K/K_{all} is larger than 0.5, increasing K/K_{all} has limit improvement to the accuracy. In this case, it is more feasible to expand the available range of the OFDM symbol K_{all} to further enhance the CRB. Although the noise-limited sensing result has the best performance when $|f_d| > f_{d,M}$, it can be observed from the Case 1 in Fig. 4 (b) that the CRB has significant fluctuation when the velocity is close to zero, i.e., $|v| < 5\text{m/s}$. Therefore, a further optimization is required to reduce the mainlobe of the Doppler pattern, hence, the motivation of Algorithm 1.

Fig. 8 evaluates the impact of the small-amount perturbation of $\tilde{\varphi}$ on the envelope $\mathcal{E}_{\mathcal{P}}(\tilde{\varphi}, f_d)$, as illustrated in Proposition 5. We see that the mainlobe and nearby sidelobes of $\mathcal{E}_{\mathcal{P}}(\tilde{\varphi}, f_d)$, have minimal changes with or without the perturbation on $\tilde{\varphi}$. This verifies Proposition 5 and the feasibility of Algorithm 1.

Fig. 9 displays the interference-limited Doppler sensing CRB using Algorithm 1, where $K_{\text{all}} = 512$ and 1024 for Figs. 9 (a) and 9 (b), respectively. As benchmark performances, Figs. 9 (a) and 9 (b) plot the CRB under the noise-limited Doppler sensing method given in Proposition 3. We see that both the benchmark CRB results have large values when $|v| < 5\text{m/s}$, indicating poor sensing performances of a dynamic target. Algorithm 1 is proposed to reduce the mainlobe of the envelope $\mathcal{E}_{\mathcal{P}}(\tilde{\varphi}, f_d)$ to reduce the CRB. Fig. 9 validates the effectiveness of Algorithm 1. We see that the CRB values are substantially reduces between $1\text{m/s} < |v| < 5\text{m/s}$ in Fig. 9 (a) and between $0.5\text{m/s} < |v| < 5\text{m/s}$ in Fig. 9 (b). The CRB values are increased in the sidelobe regions but only slightly. Moreover, the observable velocity range for the cases $K = K_{\text{all}} = 512$

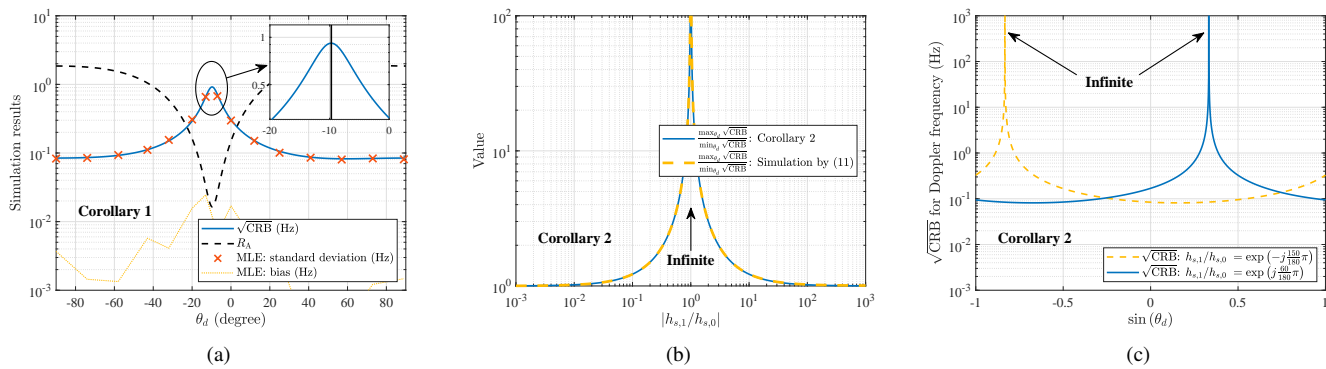


Fig. 5. Doppler CRBs (11) for Doppler versus θ_d . (a) Doppler CRBs versus θ_d ; (b) Results of (18c) versus $|h_{s,1}/h_{s,0}|$; (c) Doppler CRBs versus $\sin(\theta_d)$.

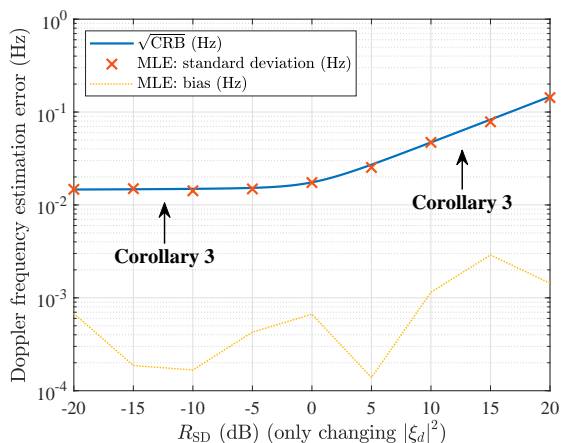


Fig. 6. Doppler CRBs (11) and the MLE results versus R_{SD} .

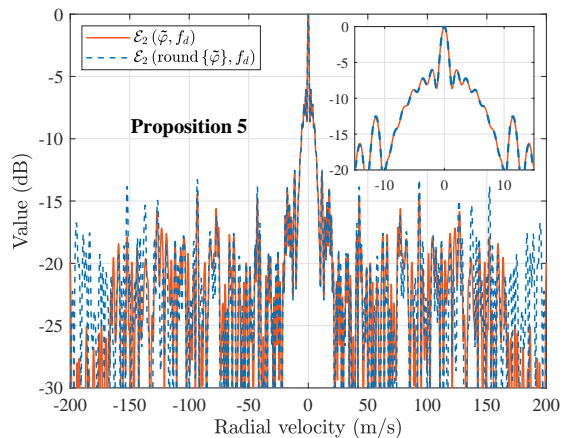


Fig. 8. Comparison of $\mathcal{E}_{\mathcal{P}}(\tilde{\varphi}, f_d)$ and $\mathcal{E}_{\mathcal{P}}(\text{round}\{\tilde{\varphi}\}, f_d)$.

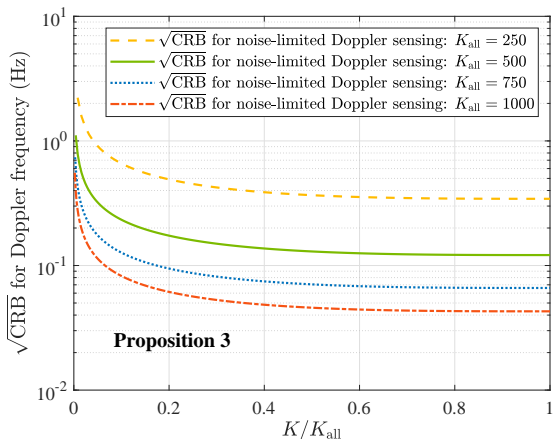


Fig. 7. Doppler CRB (11) of the proposed noise-limited Doppler sensing method in Proposition 3 versus K/K_{all} .

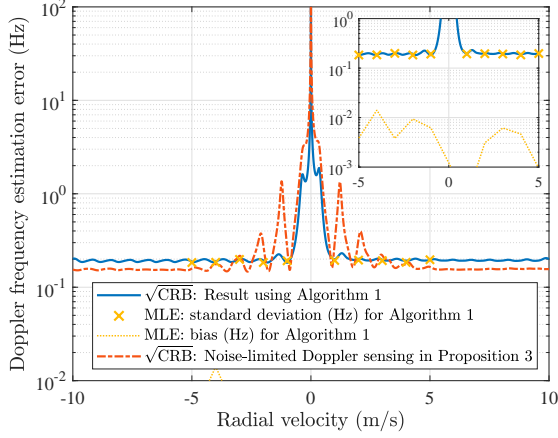
and $K = K_{\text{all}} = 1024$ is $|v| > 0.8\text{m/s}$ and $|v| > 0.4\text{m/s}$, respectively, as can be seen in Fig. 9. We also provide the MLE results in Fig. 9. Results show that the interference-limited Doppler sensing CRB using Algorithm 1 is not only the theoretical CRB but also achievable in both figures.

Fig. 10 displays the CRB results under different K_F . Recall

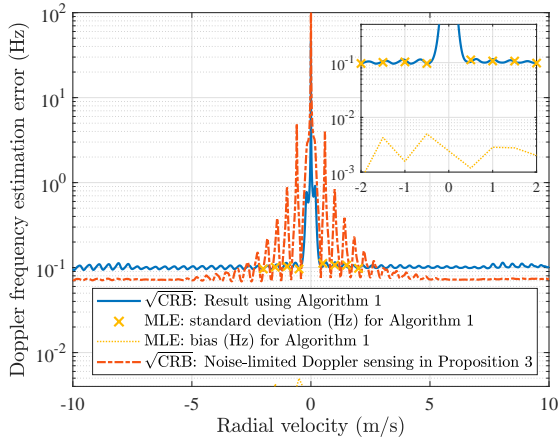
that the term K_F denotes the number of the fixed OFDM symbols which are not used in the waveform optimization; see also Fig. 2. From Fig. 10, we see that, when K_F is reduced, the sidelobe of the CRB increases, while the mainlobe level increases. This is expected, since the fixed OFDM symbols are used to ensure that the CRB in the sidelobe region of the Doppler pattern is low. On the contrary, less fixed OFDM symbols lead to more symbols available for optimization, as illustrated in Fig. 2. Therefore, the mainlobe level of the CRB decreases. Fig. 10 validates that K_F provides an extra degree of freedom for handling practical requirements in waveform optimization.

VI. CONCLUSION

In this paper, we derive the CRB of the CSI-ratio model in high-SNR and single-dynamic-target case. For simplifying the analysis and the optimization, we have provided a concise closed-form approximation of the Doppler CRB, using which we analyze the influence of each parameter on the model accuracy. Then, we enhance the accuracy of the Doppler CRB by optimizing the OFDM symbol index. We first propose the noise-limited Doppler sensing method with the Doppler CRB optimization. However, the model accuracy for the dynamic target with low-Doppler is obviously poor. We have



(a)



(b)

Fig. 9. Comparison of the noise-limited CRB result using Proposition 3, the interference-limited CRB result using the proposed Algorithm 1, and the MLE results for Algorithm 1, with (a) $K_{\text{all}} = 512$, $K = 128$, and $K_F = 16$, and (b) $K_{\text{all}} = 1024$, $K = 128$, and $K_F = 16$.

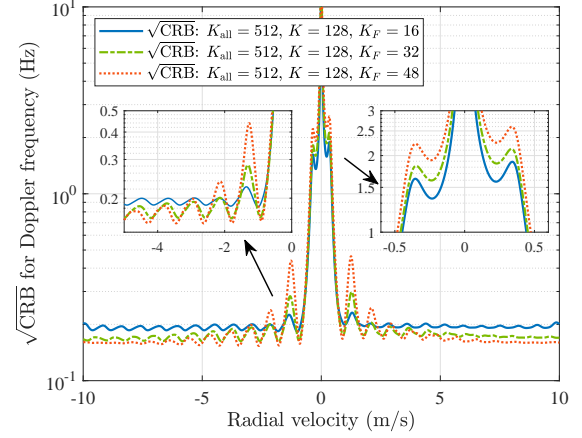
then proposed an OFDM symbol optimization algorithm in Algorithm 1 to reduce the CRB at low-Doppler range. Simulation results verify the correctness of the derivation and the analysis.

For future work, we can improve the CSI ratio performance by selecting the best pairs of antennas and the best subcarriers for sensing since the CRB result is related to the antenna and subcarrier indexes. We can also extend the work to the case of joint sensing using multiple subcarriers.

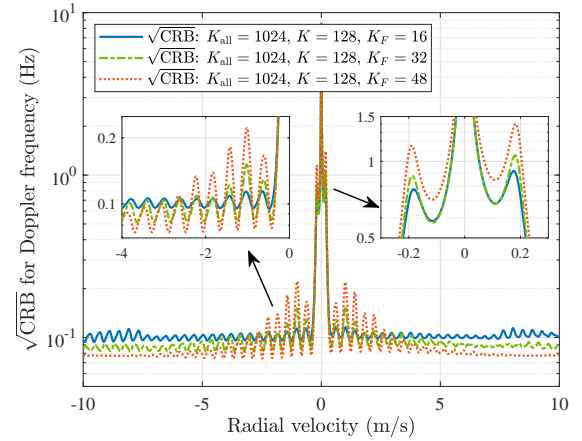
APPENDIX A PROOF OF PROPOSITION 1

The partial derivative of χ with respect to each element in α , as defined in (8), can be calculated as:

$$\begin{aligned} \frac{\partial \chi}{\partial f_d} &= j2\pi T_0 \rho_1 \text{diag}\{\varphi\} \frac{\mathbf{d}(f_d)[a(\theta_d) - \rho_0]}{(\rho_1 \mathbf{d}(f_d) + \mathbf{1}_{K \times 1})^2} \\ \frac{\partial \chi}{\partial \theta_d} &= \rho_1 \frac{\partial a(\theta_d)}{\partial \theta_d} \frac{\mathbf{d}(f_d)}{\rho_1 \mathbf{d}(f_d) + \mathbf{1}_{K \times 1}} \\ \frac{\partial \chi}{\partial \text{Re}\{\rho_0\}} &= \frac{\mathbf{1}_{K \times 1}}{\rho_1 \mathbf{d}(f_d) + \mathbf{1}_{K \times 1}} = -j \frac{\partial \chi}{\partial \text{Im}\{\rho_0\}} \end{aligned}$$



(a)



(b)

Fig. 10. Comparison of the optimal CRB results using proposed Algorithm 1 under different K_F : (a) $K_{\text{all}} = 512$, $K = 128$; (b) $K_{\text{all}} = 1024$, $K = 128$.

$$\frac{\partial \chi}{\partial \text{Re}\{\rho_1\}} = \frac{\mathbf{d}(f_d)[a(\theta_d) - \rho_0]}{(\rho_1 \mathbf{d}(f_d) + \mathbf{1}_{K \times 1})^2} = -j \frac{\partial \chi}{\partial \text{Im}\{\rho_1\}}. \quad (32)$$

Substituting (32) into (10), we can obtain the FIM of the parameters, denoted as \mathbf{F} . Utilizing the Schur complement, the inverse of the FIM can be expressed as:

$$\begin{aligned} \mathbf{C}(\alpha) &= \mathbf{F}^{-1} \\ &\triangleq \begin{bmatrix} \mathbf{F}_{11} \in \mathbb{R}^{2 \times 2} & \mathbf{F}_{12} \in \mathbb{R}^{2 \times 4} \\ \mathbf{F}_{12}^T \in \mathbb{R}^{4 \times 2} & \mathbf{F}_{22} \in \mathbb{R}^{4 \times 4} \end{bmatrix}^{-1} = \begin{bmatrix} \mathbf{H}^{-1} & \times \\ \times & \times \end{bmatrix}, \quad (33) \end{aligned}$$

where $\mathbf{H} = \mathbf{F}_{11} - \mathbf{F}_{12} \mathbf{F}_{22}^{-1} \mathbf{F}_{12}^T$. Using (33), the result given in (12) can be obtained. Proposition 1 is thus proved.

APPENDIX B PROOF OF PROPOSITION 2

From the CRB derived in Appendix A, there are nine key terms, i.e., ε_1 , $\varepsilon_{K,1}$, $\varepsilon_{K,2}$, $\varepsilon_{\mu,1}$, $\varepsilon_{\mu,2}$, $\varepsilon_{d,\mu,2}$, $\varepsilon_{d,\mu,1}$, $\varepsilon_{K,\mu}$, and $\varepsilon_{d,K,\mu}$, as given in (13). Here, we derive the approximation of ε_1 as an example. Before further derivations, we provide the following lemma, with its proof established in Appendix C.

Lemma 2. Let $\phi \in [-\pi, \pi]$ be a constant. When $|f_d| > f_{d,M}$ and $b_0 > 2b_1$, we have the following approximation:

$$\mathcal{L}_{f_d}(b_0, b_1) = \sum_{k=0}^{K-1} \frac{1}{b_0 + b_1 \cos(2\pi\varphi_k T_0 f_d + \phi)} \approx \frac{K}{\sqrt{b_0^2 - b_1^2}}. \quad (34)$$

Based on the definition of ε_1 in (13), we have:

$$\begin{aligned} \varepsilon_1 &= \sum_{k=0}^{K-1} \frac{1}{|\rho_1 e^{j2\pi k f_d T_0} + 1|^2 + |\rho_1 e^{j2\pi k f_d T_0} + \rho_0 a^*(\theta_d)|^2} \\ &= \sum_{k=0}^{K-1} \frac{1}{|\rho_0|^2 + 2|\rho_1|^2 + 1 + 2\operatorname{Re}\{[1 + \rho_0^* a(\theta_d)] \rho_1 e^{j2\pi k f_d T_0}\}}. \end{aligned}$$

Using Lemma 2, we can obtain $b_0^{(\varepsilon_1)} = |\rho_0|^2 + 2|\rho_1|^2 + 1$; $b_1^{(\varepsilon_1)} = 2|\rho_1 + \rho_0^* \rho_1 a(\theta_d)|$. Moreover, we can show that $b_0^{(\varepsilon_1)} > b_1^{(\varepsilon_1)}$ always holds, specifically:

$$\begin{aligned} b_0^{(\varepsilon_1)} - b_1^{(\varepsilon_1)} &= |\rho_0|^2 + 2|\rho_1|^2 + 1 - 2|[1 + \rho_0^* a(\theta_d)] \rho_1| \\ &\geq |\rho_0|^2 + 2|\rho_1|^2 + 1 - 2(|\rho_0| + 1)|\rho_1| \\ &= (|\rho_1| - 1)^2 + (|\rho_0| - |\rho_1|)^2 > 0. \end{aligned} \quad (35)$$

To meet the accuracy requirement of the approximation, we need to ensure that $b_0^{(\varepsilon_1)} > 2b_1^{(\varepsilon_1)}$ based on Lemma 2, i.e.:

$$|\rho_1|^2 \leq \frac{1}{16} (1 + |\rho_0|^2) \quad \text{or} \quad |\rho_1|^2 \geq 5 (1 + |\rho_0|^2). \quad (36)$$

Therefore, when $|f_d| > f_{d,M}$ and (36) are satisfied, the approximation of ε_1 is:

$$\varepsilon_1 \approx \mathcal{L}_{f_d}(b_0^{(\varepsilon_1)}, b_1^{(\varepsilon_1)}), \quad (37)$$

The other eight terms can be approximated using the similar method devised for ε_1 . With the details suppressed, we provide the following results for $|f_d| > f_{d,M}$:

$$\begin{aligned} \varepsilon_{K,1} &\approx S_{\varphi,1}(2\pi T_0) \varepsilon_1, & \varepsilon_{K,2} &\approx S_{\varphi,2}(2\pi T_0)^2 \varepsilon_1, \\ \varepsilon_{K,\mu} &\approx S_{\varphi,1}(2\pi T_0) \varepsilon_{\mu,1}, & \varepsilon_{d,K,\mu} &\approx S_{\varphi,1}(2\pi T_0) \varepsilon_{d,\mu,1}, \\ \varepsilon_{d,\mu,2} &\approx \varepsilon_{\mu,1}^* \varepsilon_{d,\mu,1} / \varepsilon_1, \end{aligned} \quad (38)$$

where $S_{\varphi,1} = \frac{1}{K} \mathbf{1}_{K \times 1}^T \varphi$, and $S_{\varphi,2} = \frac{1}{K} \varphi^T \varphi$.

Utilizing (38), the terms $[\mathbf{H}]_{1,1}$ and $[\mathbf{H}]_{1,2}$ can be approximated to $[\mathbf{H}]_{1,1} \approx 8\pi^2 T_0^2 \frac{|\xi_d \rho_2|^2}{\sigma_n^2} (S_{\varphi,2} - S_{\varphi,1}^2) \varepsilon_1$ and $[\mathbf{H}]_{1,2} \approx 0$, respectively. Hence, the inverse of the closed-form CRB for Doppler frequency can be calculated as:

$$\begin{aligned} \text{CRB}_{f_d}^{-1} &\approx 8\pi^2 T_0^2 \frac{|a(\theta_d) - \rho_0|^2}{\sigma_n^2 |\xi_d|^{-2}} (S_{\varphi,2} - S_{\varphi,1}^2) \varepsilon_1 \\ &= 8\pi^2 T_0^2 K (S_{\varphi,2} - S_{\varphi,1}^2) \frac{R_{\text{SN}} R_A}{\sqrt{(1 - R_{\text{SD}})^2 + 2R_A R_{\text{SD}}}}, \end{aligned} \quad (39)$$

where R_{SN} , R_{SD} , and R_A are defined in Proposition 2.

APPENDIX C PROOF OF LEMMA 2

Utilizing the property of the convolution operation, (34) can be expressed as:

$$\mathcal{L}_{f_d}(b_0, b_1) = \frac{1}{K_{\text{all}}} \sum_{\tilde{k}=0}^{K_{\text{all}}-1} X_c(\tilde{k}) \sum_{k=0}^{K-1} e^{j \frac{2\pi}{K_{\text{all}}} \varphi_k \tilde{k}}, \quad (40)$$

where $X_c(\tilde{k}) = \mathcal{F}_{\tilde{k}} \left\{ \frac{1}{b_0 + b_1 \cos(2\pi k T_0 f_d + \phi)} \right\}$, $\tilde{k} = 0, \dots, K_{\text{all}}-1$. The approximation of $X_c(\tilde{k})$ is given in (41) at the top of the next page under the assumption $b_0 > 2b_1$, where $\delta(\tilde{k}) = 1$ if $\tilde{k} = 0$ and $\delta(\tilde{k}) = 0$ if $\tilde{k} \neq 0$. In the first step of (41), we use the relationship $(1+x)^{-1} = \sum_{n=0}^{\infty} (-1)^n x^n$. In the second step, we expand $\cos^n(\cdot)$ using the binomial theorem. We then split the second step into two terms according to the parity of n and get the third step. Then, a key approximation is made in the third step by remaining $r = n$ in the first term and $r = n \pm 1$ in the second term based on the assumption $b_0 > 2b_1$, and we get the fourth step. In the fifth step, the relationship $(1-x)^{-\frac{1}{2}} = \sum_{n=0}^{\infty} \left(\frac{1}{4}x\right)^n C_{2n}^n$ is utilized.

Substituting (41) into (40), we have:

$$\begin{aligned} \mathcal{L}_{f_d}(b_0, b_1) &\approx \frac{K}{\sqrt{b_0^2 - b_1^2}} \\ &- K \operatorname{Re} \left\{ \frac{e^{j\phi}}{K} \sum_{k=0}^{K-1} e^{j2\pi\varphi_k T_0 f_d} \right\} \sum_{n=0}^{\infty} \frac{b_1^{2n+1}}{2^{2n} b_0^{2n+2}} C_{2n+1}^n, \end{aligned} \quad (42)$$

where $\operatorname{Re} \left\{ \frac{e^{j\phi}}{K} \sum_{k=0}^{K-1} e^{j2\pi\varphi_k T_0 f_d} \right\}$ is related with $\mathcal{P}(\varphi, f_d)$ defined in Section III-B. It can be easily proved that $\operatorname{Re} \left\{ \frac{e^{j\phi}}{K} \sum_{k=0}^{K-1} e^{j2\pi\varphi_k T_0 f_d} \right\} \leq \mathcal{P}(\varphi, f_d)$. Therefore, the mainlobe width of $\mathcal{P}(\varphi, f_d)$ can be utilized to describe the mainlobe of $\operatorname{Re} \left\{ \frac{e^{j\phi}}{K} \sum_{k=0}^{K-1} e^{j2\pi\varphi_k T_0 f_d} \right\}$. Focusing on the sidelobe, which is $|f_d| > f_{d,M}$, the second term of (42) can be eliminated, and (34) is obtained.

APPENDIX D PROOF OF PROPOSITION 4

Substituting $\varphi = [\tilde{\varphi}^T, K_{\text{all}}-1 - \tilde{\varphi}^T]^T$ into $\mathcal{P}(\varphi, f_d)$ yields:

$$\begin{aligned} \mathcal{P}(\varphi, f_d) &= \frac{1}{K} \left| \sum_{k=0}^{\frac{K}{2}-1} e^{j2\pi[\tilde{\varphi}]_k T_0 f_d} + e^{j2\pi(K_{\text{all}}-1)T_0 f_d} \sum_{k=0}^{\frac{K}{2}-1} e^{-j2\pi[\tilde{\varphi}]_k T_0 f_d} \right| \\ &= \frac{2}{K} \operatorname{Re} \left\{ e^{-j\pi(K_{\text{all}}-1)T_0 f_d} \sum_{k=0}^{\frac{K}{2}-1} e^{j2\pi[\tilde{\varphi}]_k T_0 f_d} \right\} \\ &= \operatorname{Re} \left\{ e^{-j\pi(K_{\text{all}}-1)T_0 f_d + j\angle\{\mathcal{E}_{\mathcal{P}}(\tilde{\varphi}, f_d)\}} \right\} \mathcal{E}_{\mathcal{P}}(\tilde{\varphi}, f_d) \\ &= \cos(\pi(K_{\text{all}}-1)T_0 f_d - \angle\{\mathcal{E}_{\mathcal{P}}(\tilde{\varphi}, f_d)\}) \mathcal{E}_{\mathcal{P}}(\tilde{\varphi}, f_d), \end{aligned} \quad (43)$$

where $\mathcal{E}_{\mathcal{P}}(\tilde{\varphi}, f_d)$ is the envelope of $\mathcal{P}(\varphi, f_d)$, and $\mathcal{P}(\varphi, f_d)$ is modulated by $\cos(\pi(K_{\text{all}}-1)T_0 f_d - \angle\{\mathcal{P}(\tilde{\varphi}, f_d)\})$, i.e., a ‘‘high-frequency oscillating signal’’. Proposition 4 is proved.

$$\begin{aligned}
X_c(\tilde{k}) &= \sum_{n=0}^{\infty} \frac{(-b_1)^n}{b_0^{n+1}} \mathcal{F}_{\tilde{k}} \left\{ \cos^n(2\pi k T_0 f_d + \phi) \right\} = \sum_{n=0}^{\infty} \frac{(-b_1)^n}{2^n b_0^{n+1}} \sum_{r=0}^n C_n^r \mathcal{F}_{\tilde{k}} \left\{ e^{j(2r-n)(2\pi k T_0 f_d + \phi)} \right\} \\
&= \sum_{n=0}^{\infty} \frac{(-b_1)^{2n}}{2^{2n} b_0^{2n+1}} \sum_{r=0}^{2n} C_{2n}^r \mathcal{F}_{\tilde{k}} \left\{ e^{j(2r-2n)(2\pi k T_0 f_d + \phi)} \right\} + \sum_{n=0}^{\infty} \frac{(-b_1)^{2n+1}}{2^{2n+1} b_0^{2n+2}} \sum_{r=0}^{2n+1} C_{2n+1}^r \mathcal{F}_{\tilde{k}} \left\{ e^{j(2r-2n-1)(2\pi k T_0 f_d + \phi)} \right\} \\
&\approx \sum_{n=0}^{\infty} \frac{b_1^{2n}}{2^{2n} b_0^{2n+1}} \sum_{r=n}^n C_{2n}^r \mathcal{F}_{\tilde{k}} \left\{ e^{j(2r-2n)(2\pi k T_0 f_d + \phi)} \right\} - \sum_{n=0}^{\infty} \frac{b_1^{2n+1}}{2^{2n+1} b_0^{2n+2}} \sum_{r=n}^{n+1} C_{2n+1}^r \mathcal{F}_{\tilde{k}} \left\{ e^{j(2r-2n-1)(2\pi k T_0 f_d + \phi)} \right\} \\
&= \frac{K_{\text{all}}}{\sqrt{b_0^2 - b_1^2}} \delta(\tilde{k}) - \mathcal{F}_{\tilde{k}} \left\{ \cos(2\pi k T_0 f_d + \phi) \right\} \sum_{n=0}^{\infty} \frac{b_1^{2n+1}}{2^{2n} b_0^{2n+2}} C_{2n+1}^n. \tag{41}
\end{aligned}$$

APPENDIX E

PROOF OF PROPOSITION 5

Suppose that $\tilde{\varphi}'_B = \tilde{\varphi}_B + \delta_B$, where $\delta_B \in \mathbb{R}^{K_B \times 1}$ and $|\delta_B| \leq \frac{1}{2} \mathbf{1}_{K_B \times 1}$. We have:

$$\begin{aligned}
&\left| \mathcal{E}_{\mathcal{P}} \left(\begin{bmatrix} \tilde{\varphi}_F \\ \tilde{\varphi}_B \end{bmatrix}, f_d \right) - \mathcal{E}_{\mathcal{P}} \left(\begin{bmatrix} \tilde{\varphi}_F \\ \tilde{\varphi}_B + \delta_B \end{bmatrix}, f_d \right) \right| \\
&\leq \left| \frac{2}{K} \sum_{k=0}^{K_B-1} e^{j2\pi[\tilde{\varphi}_B]_k T_0 f_d} \left\{ 1 - e^{j2\pi[\delta_B]_k T_0 f_d} \right\} \right| \\
&\approx \left| \frac{2}{K} 2\pi T_0 f_d \sum_{k=0}^{K_B-1} [\delta_B]_k e^{j2\pi[\tilde{\varphi}_B]_k T_0 f_d} \right| \\
&< \left| \frac{2}{K} 2\pi T_0 f_d \sum_{k=0}^{K_B-1} \frac{1}{2} \right| = \frac{\pi K_B}{K/2} |T_0 f_d|. \tag{44}
\end{aligned}$$

Proposition 5 is thus proved.

APPENDIX F

PROOF OF (29)

When $\mathcal{H}_{\text{op}}^{(i+1)}$ is minimized, the partial derivative of $\mathcal{H}_{\text{op}}^{(i+1)}$ with respect to $\Delta\tilde{\varphi}_B^{(i+1)}$ is zero, i.e., $\frac{\partial}{\partial \Delta\tilde{\varphi}_B^{(i+1)}} \mathcal{H}_{\text{op}}^{(i+1)} = 0$, which leads to:

$$\frac{\partial}{\partial \Delta\tilde{\varphi}_B^{(i+1)}} \mathcal{P}_{\text{SL}}^{(i+1)} + 2a \text{diag} \left\{ \mathbf{w}^{(i)} \right\} \Delta\tilde{\varphi}_B^{(i+1)} = 0. \tag{45}$$

Given the relationship between \mathcal{P}_{SL} and $\mathcal{E}_{\mathcal{P}}(\tilde{\varphi}, f_d)$ in (23), the partial derivative of $|\mathcal{E}_{\mathcal{P}}(\tilde{\varphi}^{(i+1)}, f_d)|^2$ with respect to $\Delta\tilde{\varphi}_B^{(i+1)}$ is needed for deriving the first term on the left-hand side above. Based on (23), we can show that:

$$\begin{aligned}
&\frac{\partial}{\partial \Delta\tilde{\varphi}_B^{(i+1)}} \left| \mathcal{E}_{\mathcal{P}}(\tilde{\varphi}^{(i+1)}, f_d) \right|^2 \\
&= -2f_d \frac{8\pi T_0}{K^2} \text{Im} \left\{ \mathbf{f} \left(\tilde{\varphi}_B^{(i)}, f_d \right) \mathbf{f}^H \left(\tilde{\varphi}_B^{(i)}, f_d \right) \right\} \mathbf{1}_{K/2 \times 1} \\
&+ 2f_d^2 \frac{4(2\pi T_0)^2}{K^2} \text{Re} \left\{ \mathbf{f} \left(\tilde{\varphi}_B^{(i)}, f_d \right) \mathbf{f}^H \left(\tilde{\varphi}_B^{(i)}, f_d \right) \right\} \Delta\tilde{\varphi}_B^{(i+1)}. \tag{46}
\end{aligned}$$

Substituting (46) into the first term of (45) yields:

$$\begin{aligned}
\frac{\partial}{\partial \Delta\tilde{\varphi}_B^{(i+1)}} \mathcal{P}_{\text{SL}}^{(i+1)} &= \int_{f_{d,M}^{\text{ex}}}^{\frac{1}{2T_0}} \varpi(f_d) \frac{\partial |\mathcal{E}_{\mathcal{P}}(\tilde{\varphi}^{(i+1)}, f_d)|^2}{\partial \Delta\tilde{\varphi}_B^{(i+1)}} df_d \\
&\approx 2\mathbf{V}_2^{(i)} \Delta\tilde{\varphi}_B^{(i+1)} - 2\mathbf{V}_1^{(i)} \mathbf{1}_{K/2 \times 1}, \tag{47}
\end{aligned}$$

where the definition of $\mathbf{V}_1^{(i)} \in \mathbb{C}^{K_B \times \frac{K}{2}}$ and $\mathbf{V}_2^{(i)} \in \mathbb{C}^{K_B \times K_B}$ is given in (29). Substituting (47) into (45), the formula (29) can be proved.

REFERENCES

- [1] J. A. Zhang, M. L. Rahman, K. Wu, X. Huang, Y. J. Guo, S. Chen, and J. Yuan, "Enabling joint communication and radar sensing in mobile networks-A survey," *IEEE Commun. Surveys Tuts.*, vol. 24, no. 1, pp. 306–345, 2022.
- [2] Q. Shi, L. Liu, S. Zhang, and S. Cui, "Device-free sensing in OFDM cellular network," *IEEE J. Sel. Areas Commun.*, vol. 40, no. 6, pp. 1838–1853, 2022.
- [3] F. Meneghello, D. Garlisi, N. D. Fabbro, I. Tinnirello, and M. Rossi, "Sharp: Environment and person independent activity recognition with commodity IEEE 802.11 access points," *IEEE Trans. on Mobile Comput.*, vol. 22, no. 10, pp. 6160–6175, 2023.
- [4] H. Sun, L. G. Chia, and S. G. Razul, "Through-wall human sensing with WiFi passive radar," *IEEE Trans. Aerosp. Electron. Syst.*, vol. 57, no. 4, pp. 2135–2148, 2021.
- [5] J. Pegoraro, J. O. Lacruz, T. Azzino, M. Mezzavilla, M. Rossi, J. Widmer, and S. Rangan, "Jump: Joint communication and sensing with unsynchronized transceivers made practical," 2023. [Online]. Available: <https://doi.org/10.48550/arXiv.2304.07766>
- [6] Y. Cui, F. Liu, X. Jing, and J. Mu, "Integrating sensing and communications for ubiquitous IoT: Applications, trends, and challenges," *IEEE Netw.*, vol. 35, no. 5, pp. 158–167, 2021.
- [7] J. A. Zhang, K. Wu, X. Huang, Y. J. Guo, D. Zhang, and R. W. Heath, "Integration of radar sensing into communications with asynchronous transceivers," *IEEE Commun. Mag.*, vol. 60, no. 11, pp. 106–112, 2022.
- [8] M. Ahmadi-pour, M. Wigger, and S. Shamai, "Strong converses for memoryless bi-static ISAC," in *2023 IEEE International Symposium on Information Theory (ISIT)*, 2023, pp. 1818–1823.
- [9] C. Li, N. Raymondi, B. Xia, and A. Sabharwal, "Outer bounds for a joint communicating radar (comm-radar): The uplink case," *IEEE Trans. Commun.*, vol. 70, no. 2, pp. 1197–1213, 2022.
- [10] M. L. Rahman, J. A. Zhang, X. Huang, Y. J. Guo, and R. W. Heath, "Framework for a perceptive mobile network using joint communication and radar sensing," *IEEE Trans. Aerosp. Electron. Syst.*, vol. 56, no. 3, pp. 1926–1941, 2020.
- [11] W. Yuan, N. Wu, B. Etlzinger, Y. Li, C. Yan, and L. Hanzo, "Expectation-maximization-based passive localization relying on asynchronous receivers: Centralized versus distributed implementations," *IEEE Trans. Commun.*, vol. 67, no. 1, pp. 668–681, 2019.
- [12] G. Wen, H. Song, F. Gao, Y. Liang, and L. Zhu, "Target localization in asynchronous distributed MIMO radar systems with a cooperative target," *IEEE Trans. Wireless Commun.*, vol. 21, no. 6, pp. 4098–4113, 2022.
- [13] Z. Ni, J. A. Zhang, X. Huang, K. Yang, and J. Yuan, "Uplink sensing in perceptive mobile networks with asynchronous transceivers," *IEEE Trans. on Signal Process.*, vol. 69, pp. 1287–1300, 2021.
- [14] K. Qian, C. Wu, Y. Zhang, G. Zhang, and Y. Liu, "Widar2.0: Passive human tracking with a single Wi-Fi link," *Proc. 16th Annu. Int. Conf. Mobile Syst., Appl. Serv.*, pp. 350–361, 2018. [Online]. Available: <https://doi.org/10.1145/3210240.3210314>
- [15] Y. Zeng, D. Wu, J. Xiong, E. Yi, R. Gao, and D. Zhang, "Farsense: Pushing the range limit of WiFi-based respiration sensing with CSI ratio of two antennas," in *Proc. ACM Interact. Mob. Wearable Ubiquitous Technol.*, vol. 3, no. 3, 2019.
- [16] X. Li, J. A. Zhang, K. Wu, Y. Cui, and X. Jing, "CSI-ratio-based Doppler frequency estimation in integrated sensing and communications," *IEEE Sens. J.*, vol. 22, no. 21, pp. 20 886–20 895, 2022.

- [17] Z. Ni, J. A. Zhang, K. Wu, and R. P. Liu, "Uplink sensing using CSI ratio in perceptive mobile networks," *IEEE Trans. on Signal Process.*, vol. 71, pp. 2699–2712, 2023.
- [18] S. M. Kay, *Fundamentals of Statistical Signal Processing Volume I: Estimation Theory*, (Prentice-Hall Signal Processing Series). Englewood Cliffs, NJ, USA: Prentice-Hall, 1993.
- [19] S. D. Liyanaarachchi, T. Riihonen, C. B. Barneto, and M. Valkama, "Optimized waveforms for 5G-6G communication with sensing: Theory, simulations and experiments," *IEEE Trans. Wireless Commun.*, vol. 20, no. 12, pp. 8301–8315, 2021.
- [20] M. Bie? and V. Koivunen, "Radar waveform optimization for target parameter estimation in cooperative radar-communications systems," *IEEE Trans. Aerosp. Electron. Syst.*, vol. 55, no. 5, pp. 2314–2326, 2019.
- [21] Y. Li, Z. Wei, and Z. Feng, "Joint subcarrier and power allocation for uplink integrated sensing and communication system," *IEEE Sens. J.*, vol. 23, no. 24, pp. 31 072–31 081, 2023.
- [22] Y. Hu, W. Deng, J. A. Zhang, and Y. J. Guo, "Resource optimization for delay estimation in perceptive mobile networks," *IEEE Wireless Commun. Lett.*, pp. 1–1, 2023.
- [23] G. Noh, B. Hui, J. Kim, H. S. Chung, and I. Kim, "DMRS design and evaluation for 3GPP 5G new radio in a high speed train scenario," in *Proc. IEEE GLOBECOM 2017-IEEE Glob. Commun. Conf.*, 2017, pp. 1–6.
- [24] 3GPP TS 38.213, Physical channels and modulation, V15.2.0, January 2023.
- [25] X. Lin, J. Li, R. Baldemair, J.-F. T. Cheng, S. Parkvall, D. C. Larsson, H. Koorapaty, M. Frenne, S. Falahati, A. Grovlen, and K. Werner, "5G New Radio: Unveiling the essentials of the next generation wireless access technology," *IEEE Commun. Stand. Mag.*, vol. 3, no. 3, pp. 30–37, 2019.
- [26] D. E. Francs and F. J. Rubio, "On the existence of a normal approximation to the distribution of the ratio of two independent normal random variables," *Statist. Papers*, vol. 54, pp. 309–323, 2013.
- [27] G. Buttazzoni and R. Vescovo, "Reducing the sidelobe power pattern of linear broadside arrays by refining the element positions," *IEEE Antennas Wireless Propag. Lett.*, vol. 17, no. 8, pp. 1464–1468, 2018.